Identification of diagenetic overprint and recrystallization of foraminiferal shell calcite by Electron Backscattered Diffraction (EBSD)

Anna Sancho Vaquer[1], Erika Griesshaber[1], Julie Meilland[2], Xiaofei Yin[1,3], Michael Siccha[4], Michal Kucera[4], and Wolfgang W. Schmahl[1]

5

[1]Department of Earth and Environmental Sciences, LMU Munich, Munich, 80333, Germany
[2]CEREGE – Environmental Geosciences Research and Teaching Centre, French National Centre for Scientific Research, Aix-en-Provence, 13545, France
[3]Bruker Nano Surfaces and Metrology Division, Minhang District, Shanghai, 200233, China
10 [4]MARUM – Centre for Marine Environmental Sciences, University of Bremen, Bremen, 28359, Germany

Correspondence to: Anna Sancho Vaquer (a.sancho@campus.lmu.de)

Abstract. Electron backscatter diffraction (EBSD) measurements and data evaluation render the mode of crystal organization in the scanned sample volume, many crystallographic attributes of the comprising crystals and structural information of the entire hard tissue. Knowledge is gained on crystal microstructure, crystal texture, degree of misorientation

15 and/or co-orientation between crystals, crystal-twin-formation, among others. As foraminiferal Ca-carbonate records chemical and physical parameters of the ambient environment, the shells serve as archives for environmental and climate change. However, the recorded information is often biased due to the alteration of shell Ca-carbonate by dissolution, precipitation, recrystallization, and the transformation of the biocrystals into their inorganic analogues.

We demonstrate that the diagenetic overprint of foraminiferal Ca-carbonate can be identified using structural characteristics

20 measured with EBSD and information obtained from the corresponding data evaluation. We investigated modern/pristine and fossil *Trilobatus sacculifer* shells and highlighted an undisturbed shell surface for both. Nevertheless, we demonstrate that there is an increase in recrystallized calcite in the shells and a decrease in pristine, twinned calcite with increasing fossilization. We show that crystal microstructure and texture, and the frequency of the 60°-{001}-twin-misorientation and other misorientations are modified with an increasing degree of overprint. We propose the use of structural attributes

25 provided by EBSD to identify recrystallized/overprinted foraminiferal carbonate. Highlighting low degrees of overprint is of main importance as, in contrast to strong overprint, small structural changes of overprinted shells are easily overlooked with SEM-imaging, while even a minute change of shell microstructure and texture is easily identified with EBSD measurements.

1 Introduction

Paleoclimatic and paleoenvironmental reconstructions are largely based on biologically secreted Ca-carbonate archives and

30 the proxies (chemical, physical) that disclose the climate and environment information from archival hard tissue (Akhtar et al., 2024; Brand et al., 2003; Carpenter and Lohmann, 1995; Fantle et al., 2020; Immenhauser et al., 2016; Kramer et al.,

2010; Pearson, 2012; Sandberg, 1983; Schöne et al., 2011; Stolper et al., 2018; Swart, 2015; Veizer et al., 1999; Ye et al., 2019; Zachos et al., 1994, 2001). The mineralization of the structural biomaterial environmental signals become incorporated into the hard tissue in a systematic, biologically controlled way (Brand, 2004; Casella et al., 2018a, b; Ku et al., 1999; Ye et al., 2018). However, this notion is only valid at the so-called metabolic equilibrium, when the Ca-carbonate producing organism is alive and is secreting the biomineralized soft and hard tissues (Casella et al., 2018a, b; Simonet Roda et al., 2019; Ye et al., 2021). After the death of the organism, metabolic equilibrium is not sustained anymore and the biomineralized tissues transform toward non-biological thermodynamic equilibrium. The biomineralized soft and hard tissues become subject to changes in organic substance fabric and content, crystal mosaic structure, crystal microstructure and crystal chemistry. These changes result from decay, dissolution, precipitation and recrystallization (Casella et al., 2017, 2018a, b; Putnis, 2009; Putnis and Austrheim, 2013; Ye et al., 2021). Accordingly, the pristine environmental signatures recorded by the archival tissue at biomineralization are modified; in some cases, ambient information is only slightly distorted, in others, it is completely changed.

Benthic and planktonic foraminifera are key producers of pelagic carbonate sediments, and their shells are major archives of climate and environment information. The latter is disclosed with shell chemistry, acting as geochemical proxies for water composition, water pollution and ecological characteristics (Chanda et al., 2019; Fantle et al., 2020; Sancho Vaquer et al., 2025a; Stainbank et al., 2021; Stewart et al., 2015; Veizer et al., 1999). Nonetheless, the fidelity of all geochemical and shell-related proxies is based on the assumption that there is either minimal or no exchange between secreted shell carbonate and water chemistry. However, research of the last decades has shown that this is not the case. Numerous studies demonstrated that geochemical proxies (e.g., Mg/Ca, $\delta^{18}O$) are strongly susceptible to alteration, called forth from the fact that the archival shell becomes quickly overprinted if not sampled alive (Chanda et al. 2019; Stainbank et al. 2021, and references therein). Edgar et al. (2013, 2015) described that the structure and chemical composition of foraminifera shells are modified by three main overprint processes: (i) overgrowth of the shell with abiogenic crystals, (ii) partial dissolution of shell crystals, and (iii) crystallization of abiogenic crystals into voids and cavities of the shell. Hence, the reliability of geochemical proxies and of the environmental information that can be obtained from the shells depends on the extent and the mode of overprint of the archive. Highlighting a low degree of overprint is most important, as is easily overlooked (Forjanes et al., 2022). In contrast, strong overprint of the shell material is well-observable, either by the absence of the shell-derived organic substance due to by decay or the marked destruction of the original crystal microstructure and texture (Casella et al., 2017, 2018a, b; Ye et al., 2021).

Analytical techniques used for the recognition of diagenetic overprint of foraminifera shells (see review of Fehrenbacher et al. (2024)) include shell structure imaging with visible light, SE and BSE electron microscopies (Hansen, 1999; Hottinger, 2006; Lipps, 1973; Nagai et al., 2018a, b; Spero, 1988; Tyszka et al., 2019) and analysis of shell mineralogy with X-ray diffraction (de Araújo et al., 2025; Bassinot et al., 2004; Nouet and Bassinot, 2007). They also include the application of chemical techniques, such as cathodoluminescence imaging (Baumgartner-Mora, 1994; Wendler et al., 2012), energy dispersive X-ray spectroscopy (Hidayat et al., 2025; Procter et al., 2024) and major and trace element chemistry and isotope

composition (Akhtar et al., 2024; Bernard et al., 2017; Charrieau et al., 2023; Cisneros-Lazaro et al., 2022; Elderfield et al., 2002; Gussone et al., 2009; Heuser et al., 2005; Hoogakker et al., 2024; Pearson, 2012; Piasecki et al., 2019; Poirier et al., 2021; Stewart et al., 2015). In a recent study, Procter et al. (2024) combined microdiffraction and energy dispersive X-ray spectroscopy techniques for the assessment of overprint of "glassy" and "frosty" planktonic foraminifera shells. They gained

70 information on shell microstructure and shell chemistry preservation.

It is necessary to perform microdiffraction measurements with a spatial resolution well below 500nm for the detection of subtle changes in crystal organization. Lastam et al. (2023a,b), Sancho Vaquer et al. (2025a, b,c), Schmahl et al. (2025), and Yin et al. (2021) utilized high-resolution electron backscatter diffraction (EBSD) to decipher the crystallographic aspects of modern/pristine rotaliid and robertinid shell calcite and aragonite. Electron backscatter diffraction measures the orientation

75 of all its crystallographic axes for a given crystal and therefore enables the measurement of crystal-microstructure and crystal-texture in the scanned sample volume. EBSD measurements not only provide the microstructure and texture of the crystallized material, but also yield a wealth of further structural information of the hard tissue in question. We also obtain information on crystal size and morphology, the degree of crystal co- and misorientation, the range of co- and misorientations between the crystals in the scanned sample volume, and the mode of crystal misorientation distribution. In

80 particular, we are able to measure the formation of specific misorientations, e. g., crystal twin-related, misorientations (Hoerl et al., 2024a; Hoerl, 2025; Lastam et al., 2023a, b; Sancho Vaquer et al., 2025b; Schmahl et al., 2025; Schwartz et al., 2000; Yin et al., 2021). When present, these are a structural attribute specific for the material in question. The above-mentioned hard tissue-related structure characteristics are gained through EBSD data evaluation and allow an in-depth and full structural characterization of the material in question (Schwartz et al., 2000).

85 Studies investigating crystal microstructure and crystal texture of modern/pristine benthic and planktonic Rotaliida and modern/pristine benthic Robertinida with EBSD demonstrated that modern/pristine rotaliid and robertinid shells exhibit one specific structural feature. The calcite of the Rotaliida and the aragonite of the Robertina are twinned according to the 60° <001> twin law in the case of calcite (Lastam et al., 2023a, b; Sancho Vaquer et al., 2025a, b; Schmahl et al., 2025) and according to the 64° {110} twin law for aragonite. Twin formation in Ca-carbonate biomaterials is wide-spread and occurs

90 predominantly in biological aragonites (Almagro et al., 2016; Crippa et al., 2020a, b; Griesshaber et al., 2013; Kogure et al., 2014; Suzuki et al., 2012). Crystal twin formation has not been reported for other biological calcites far, with the exception of the rotaliid shells (Sancho Vaquer, 2026) and of coral sclerites (Floquet and Vielzeuf, 2011). Accordingly, secretion of twinned calcite for shell construction is an intrinsic structural property of the Globothalamea. It is a structural marker for the shells of Rotaliida and Robertinida (Sancho Vaquer et al., 2025a, b Sancho Vaquer 2026).

95 In the present study, we discuss the effect of diagenetic overprint on foraminifera shells and constrain overprint with crystallographic attributes. We not just examine the integrity and/or structural change of the shell surface but use the crystallographic characteristics of the shell crystals, such as the mode of crystal assembly (crystal-microstructure and crystal-texture) and, in particular, the frequency of the twin-related misorientation peak and the frequencies of the low-angle misorientations for the identification of shell structure change. We complement crystallographic attributes of the shell

crystals with FE-SEM imaging of the shell internal structure. We investigate the effect of diagenesis for the shell of the
planktonic rotaliid species *Trilobatus sacculifer* (Brady, 1877). *T. sacculifer* is the main representative of a long-lived
lineage and *sacculifer* is one of the main species used for environmental reconstruction. Its ecological preference remained
throughout the geological record largely unchanged (Spezzaferri et al., 2015).

To characterise the effect of diagenesis on fossil shell crystal characteristics, we first determined crystallographic attributes
of modern/pristine *T. sacculifer* shells, which are used as a reference. The modern/pristine shells were obtained from
sediment traps and from the sediment surface. For identifying shell structure difference between geographical sites, we
investigated modern/pristine *T. sacculifer* shells from the East Pacific, the Central and East Atlantic Ocean, and the
Caribbean Sea. Fossil shells were extracted from different Pleistocene and Neogene sediment depths of ODP Site 927,
located on Ceara Rise, Central Atlantic Ocean. The fossil shells were obtained from 6m, 15m, 109m and 308m sediment
depth and represent a gradient in diagenetic overprint induced by a combination of increasing burial depth and increasing
age. The sampling approach used ensures that the modern/pristine as well as the fossil shells were biomineralized under
comparable environmental conditions. Reasons for the latter are the stable ecology of the long-lived species and the tropical
location of the fossil material. Nonetheless, it should be kept in mind that our study does not discriminate between diagenetic
overprint due to age of the organism and diagenetic overprint due to burial depth.

We find a comparable and good preservation of the shell surface structure for the modern/pristine as well as for the fossil
shells. However, we find a strong difference in crystal microstructure, crystal texture, crystal co-orientation strength, the
relative frequency of the 60° <001> calcite twin-related misorientation peak and the relative frequency of all other
misorientations between the modern/pristine and the fossil shells. We highlight two overprint processes for the fossil shells,
namely crystal amalgamation and calcite recrystallization. Amalgamation and recrystallization occur within the shells as
well as at their proximal and distal surface. Based on EBSD measurements, we suggest criteria for tracing structural change
of foraminiferal shell calcite initiated by diagenetic overprint. We propose to utilize EBSD measurements and data
evaluation as an analytical tool for highlighting structural markers, as a distortion of the pristine shell crystal structure
unequivocally discloses diagenesis-related change of fossil Globothalamea calcite and aragonite.

2 Samples and Methods

2.1 Samples

We investigated the shells of modern/pristine and fossil *Trilobatus sacculifer* (Brady, 1877). The specimens were sampled
from the Central and Eastern Atlantic Ocean, from the Caribbean Sea and from the Eastern Pacific (Figs. A1, A2).

As the structure, microstructure, texture, crystal twinning and crystal misorientation pattern of modern/pristine *T. sacculifer*
shells was used as reference for the fossil samples, we investigated modern/pristine specimens from four different localities.
This ensured the assessment of a possible variability of shell microstructure and texture that could be related to a difference
in living environment. We first investigated samples from sediment traps. These are fully mineralized shells sinking through

the water column after the death of the organism; however, they remaining free from contact with the seafloor sediment. We investigated shells from the sediment-water interface, thus, from the sediment surface. This enabled to trace a possible effect of a very early diagenesis. These shells reached the seafloor and were in contact with the surrounding sediment and

135   porewaters, but remained unaffected from burial diagenesis, increasing temperature, an altered porewater chemistry, and an increase in lithostatic pressure. The fossil *T. sacculifer* samples were sampled at Ceara Rise, Central Atlantic Ocean. The shells were obtained from 6m, 15m, 109m and 308m sediment depth, corresponding to ages of 0.13, 0.3, 3.1 and 15.9 million years (Cornuault et al., 2023) and an increasing degree of diagenetic overprint (Figs. A1, A2). The fossil shells were extracted from Pleistocene and Neogene sediments from ODP Site 927. The shells exhibited good surface preservation and

140   did not show any signs of dissolution.

The investigated samples were divided into seven groups: groups 1 to 3 consisted of modern/pristine specimens, groups 4 to 7 consisted of fossil shells. For each group of shells, one specimen was used for surface imaging. Two specimens were embedded in EPON resin and sectioned and polished with microtome knives (Figs. A1, A2).

2.2 Sample preparation

145   **2.2.1 Sample preparation for imaging etched and fixed shell cross-section surfaces**

To visualize small-scale internal structures and the presence of organic material within the shells, shell cross-sections were etched. First, flat surfaces were obtained by cutting and polishing the shells with a microtome with glass and trimming knives. The obtained surfaces were then simultaneously etched and fixed with a 0.1 M HEPES buffer (pH=6.5) and 2.5% glutaraldehyde solution for 120 seconds. Etching was terminated by rinsing the samples three times in 100% isopropanol for

150   10 s each. Subsequently, the samples were critical-point dried and then coated with 4–6 nm of Pt/Pd for imaging.

2.2.2 Sample preparation for EBSD measurements

Foraminifera shells were embedded in low-viscosity EPON resin and were cut and polished with an ultramicrotome with glass, trimming and diamond knives. Specimens were oriented with the primary apertures positioned towards the knife. Significant care was taken to ensure that the integrity of the shell was retained for the entire sample preparation process. This

155   ensured the assessment of a possible shell crystal dissolution. The latter might have occurred at diagenetic overprint. For EBSD measurements, the samples were coated with 4–6 nm of carbon.

2.3 Methods

SE, BSE imaging and EBSD measurements were carried out with a Hitachi SU5000 field emission SEM, equipped with an

160   Oxford Instruments NordlyNano EBSD detector and an X-Max 80x80 EDS detector. EBSD scans were performed at 20 kV, with a step size of 200 to 300 nm. EBSD data was evaluated with the Oxford Instruments AZTEC CRYSTAL and

CHANNEL 5 HKL software. Crystal orientation data are presented with color-coded crystal orientation maps, grey-scaled EBSD band contrast measurement maps, and corresponding pole figures. Each investigated specimen was scanned with at least four EBSD scans. For all these scans, we evaluated the microstructure and texture pattern of the calcite and calculated the 60°-{001}-calcite-twin misorientation as well as all other misorientations between crystals between 5° and 100°.

2.4 EBSD terminology used in this study

Subsequently, we define terms related to EBSD measurements and EBSD data evaluation, as well as the structural attributes of the crystals used in this study (Buerger, 1945; Hahn and Klapper, 2006; Richards, 1999; Schmahl et al., 2025; Schwartz et al., 2000). For further information concerning the EBSD technique, see Schwartz et al. (2000). For information related to twin formation, see Buerger (1945), Richards (1999), and Hahn and Klapper (2006).

The *microstructure* of a crystallized material refers to the sizes, morphologies, co-orientation and misorientations, and modes of interlinkage of grains. It is shown with coloured EBSD maps. Similar colours reflect similar crystal orientations, and different colours highlight differences in crystal orientation.

Pole figures are stereographic projections of crystallographic axes or plane-normal orientations measured for all pixels of an EBSD map or for selected areas (subsets). In the present contribution, the viewing direction of the pole figures is the same as the viewing direction of the corresponding EBSD maps. All pole figures shown in this study display the lower hemisphere. This ensures that the pole figures are displayed in the same spatial orientation as the corresponding EBSD map. With pole figures, we either show individual orientation data points or the density distributions of the orientation data.

The *texture* or *crystallographic preferred orientation* of a crystallized substance refers to the distribution of all crystal orientations within a material and is illustrated using pole figures. When clear-cut maxima are observed in the pole figures of all crystallographic axes, corresponding to a three-dimensional orientational ordering, we call the texture a "single-crystal-like" texture, irrespective of the angular spread of the orientation distribution. Accordingly, for calcite, we need to observe one cluster for the c-axes and three clusters for the a*-axes in the pole figure. An axial/cylindrical texture is developed in the relevant material when the c-axes show a cluster in one particular direction and the orientation of the a*-axes scatter on a great circle perpendicular to the c-axis cluster.

Crystal co-orientation statistics are derived from Kikuchi patterns measured at each pixel of an EBSD map. The degree of calcite co-orientation within individual crystals is determined from measurements of the orientational density distribution, as reflected in the multiple of uniform (random) distribution (MUD) value.

The *MUD value* is calculated by the CHANNEL 5 EBSD software and indicates the strength of crystal co-orientation. A high MUD indicates high crystal co-orientation and low MUD values indicate low to random crystallite and/or mineral unit co-orientation. The parameters for data contouring in the pole figures were fixed to a half-width of 5 and a cluster size of 3. While an MUD value of 1 indicates a polycrystalline material with random, uniform orientation distribution, a single crystal has, for a half-width of 5 and a cluster size of 3, an MUD value of 700 or higher.

195 The *EBSD band contrast measurement map* depicts the signal strength of the Kikuchi pattern at each measurement point in the EBSD scan. It is displayed as a grey-scale component in the map. White to light grey colors indicate a high intensity of the Kikuchi signal, corresponding to strong mineralization, while dark grey and black colors point to a weak or absent Kikuchi signal, e.g., when organic matter, resin, or voids are scanned.

Twinned crystals are entities in which adjacent crystals of the same phase are intergrown in a regularly recurring orientational relationship. These crystal orientation states are addressed as the *twin domains* of a *twinned crystal*. The
200 orientational relationship between twin domains is referred to as the *twin law*. Twin laws are characteristic of a mineral and are symmetry operations that define the orientation between the twin domains. Twin laws include reflection, rotation and inversion operations. If a twinned crystal contains domains of two orientation states, alternating in succession, then it is called a polysynthetic twin. In contrast to inorganic materials, in biological materials twins do not show perfectly planar and parallel composition/twin planes.

205 **3 Results**

The results section of this contribution is structured as follows: Figures A1, A2 show shell wall *cross-section surfaces* that were scanned with EBSD and/or were chemically etched, fixed, and imaged with SE and BSE. Figures 1 and 2 visualize the *surface quality* of modern/pristine and fossil shells and highlight some characteristics of the shell wall *internal structure*. Figures 3 and 4 present *microstructures* using EBSD maps of calcite. Figures 3 to 5 and A3 show the corresponding calcite
210 *texture* patterns with pole figures. Figures 3 and 4 present crystal orientation in pole figures with the individual data points. The pole figures in Figs. 5 and A3 give the density distribution of the crystal orientation data together with the *crystal co-orientation strength*, the MUD value, for the corresponding EBSD scan. Figures 6, 7 and A4 present the *misorientations* between the crystals of the investigated shells and show the encountered range of crystal misorientation. The latter were calculated from EBSD measurements and are shown with relative frequency-misorientation angle diagrams. Figures 6 and 7
215 focus on the 60° misorientation; Figure A4 shows the corresponding low-angle misorientations, thus, the misorientations between 5° and 59°.

Figure 1 juxtaposes the shell structure characteristics of a modern/pristine and of three fossil *T. sacculifer* specimens. The fossil shells were sampled at 6m, 109m and 308m sediment depth. We present the shell surface appearance and its internal structure on cross-sections through the shell wall. Even though the investigated shells appeared to be well preserved, we
220 detected subtle structural differences between the modern/pristine and the three fossil shells in: (i) shell surface structure, (ii) recognizability of the primary organic sheet (POS), (iii) internal structure of the shell wall and (iv) morphology and size of the shell wall crystals (Figs. 1A to D, 2). The honeycomb surface structure of the *T. sacculifer* shell is well observable in both the modern/pristine and fossil shells. However, the ridges surrounding the pores are more distinct for the modern/pristine shell (Fig. 1A), compared to what we find for the shells of the fossil specimens. For these, the ridges are
225 rather rounded down (Fig. 1B, C) and the pores are often filled and fully covered with sediment particles.
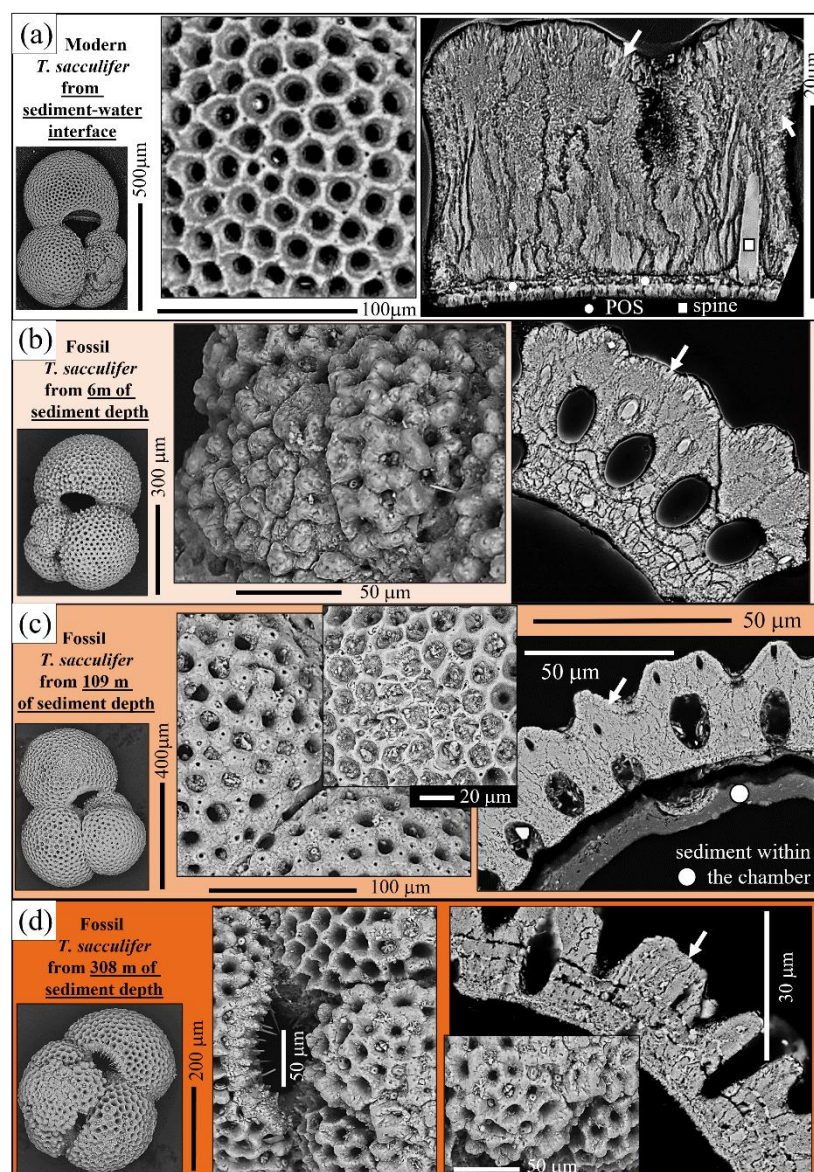
Figure 1. The shells of the investigated *T. sacculifer* specimens. A: the shell of modern/pristine *T. sacculifer*, sampled at the sediment-water interface. B to D: shells of fossil *T. sacculifer* specimens, sampled from the sediment at 6m, 109m and 308m sediment depths. We present overviews of the shells, BSE images of the shell surface, cross-section through a chamber and the internal structure of the shell walls, imaged with SE and BSE. For a better visualization of the internal shell wall structure of the modern/pristine and the fossil specimen, sampled at 308m sediment depth, see Fig. 2. The white dot in (C) points to a sediment layer within the chamber. This has often been observed for the fossil samples, see also Figs. A1 and A2. The white arrows in (A) to (D) point to the seam of calcite crystals that line the outermost section of the shell wall. A to D: BSE micrographs.

The internal structure of the shell wall is different for the modern/pristine and for the fossil shells (Fig. 2). Figure 2 juxtaposes the internal structure of the modern/pristine with that of the most overprinted shell, the shell sampled at 308m sediment depth. *T. sacculifer* shell wall crystals of the modern/pristine shell are fibrils (Fig. 2A). These are bundled and form

large crystal units (white stars in Fig. 2A). The crystals in the shell wall of the fossil shells, the ones in the fossil shells sampled at 109m and 308m sediment depth in particular, do not show any fibril appearance (compare Fig. 2A with Fig. 2B, C). In the fossil shells, the crystals are blocky and vary strongly in shape and size (e.g., Fig. 2B). The calcite of the most

240   overprinted shell (sampled at 308m depth) is compact and not as delicate as the fibril-shaped calcite of the modern/pristine shell (Fig. 2A). We observe voids within the shell for the shell sampled at 308m sediment depth (yellow arrows in Fig. 2B). These can be filled with carbonate mineral (white arrows in Fig. 2B) but can also be empty (yellow arrows in Fig. 2B). In addition, along the proximal surface of the most overprinted fossil shell, we find a dense seam of calcite crystals that have morphologies that resemble inorganic calcite rhombohedra (red arrows in Fig. 2C). The distal surface of modern/pristine *T.*

245   *sacculifer* shells is seamed by large, platy, crystals (white arrows in Fig. 1A). A seam of platy crystals is also found along the distal surface of some fossil shells of those that were sampled at 6m and 109m sediment depth (white arrow in Fig. 1B, C). For the fossil specimen sampled at 109m sediment depth, a rim along the distal surface of the shell is observable. However, platy crystals cannot be recognized anymore. With an increasing degree of overprint, the platy crystals amalgamate (white arrows in Fig. 1C, D). In the modern/pristine shell, the POS and its progression in the shell is well visible (Fig. 2A). In the

250   overprinted shells, in particular in the shells sampled at 109m and 308m sediment depth, the progression of the POS can still be traced. It is, however, badly observable (Fig. 2B, C).
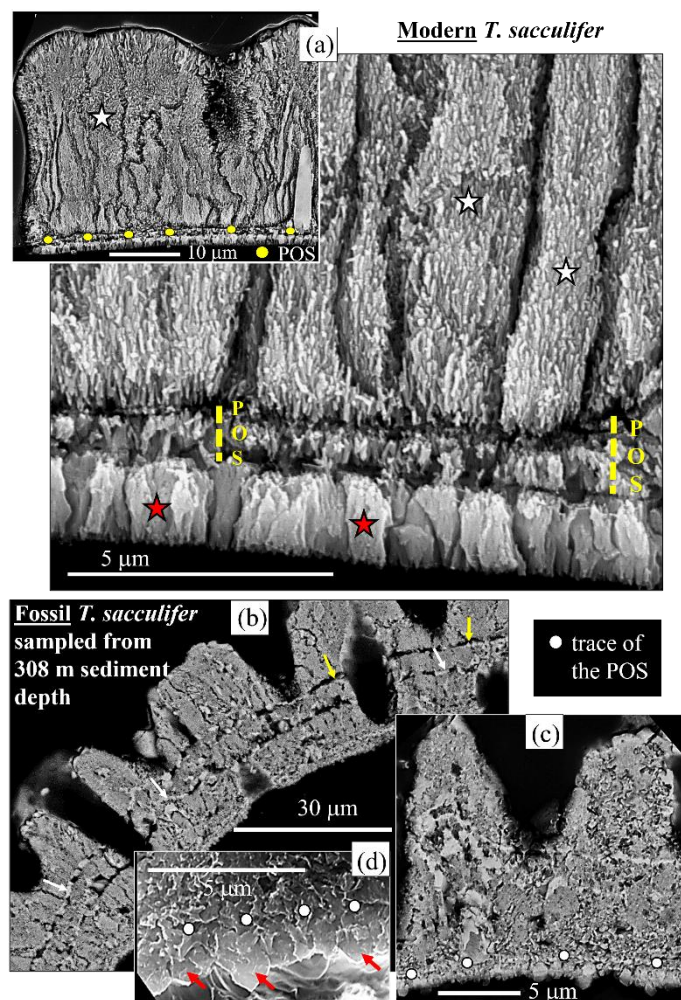
Figure 2. Calcite crystallite and crystal unit morphology and internal shell structure of a modern/pristine (A) and an overprinted (B, C, D) *T. sacculifer* shell. Note the strong difference in crystallite, crystal size and morphology (A, B, D) and the presence of fibril-shaped crystallites in the modern/pristine shell. These accumulate to co-oriented crystal units (white stars in (A)) and form large, irregularly shaped calcite entities with shell growth. The latter often cover the entire shell-wall cross-section (insert in (A)). The POS in the modern/pristine shell is well-visible. This contrasts with the fossil shell (C, D), where often, only the trace of the POS is visible. Most interesting is the accumulation of crystals that form the fossil shell proximal to the POS (red arrows in (D)). These have morphologies that resemble inorganic calcite and develop from the internally structured crystal entities (red stars in (A)) that generate the shell layer below the POS. White and yellow arrows in (B) point to voids in the fossil shell; these form when the organic substance in the shell becomes decomposed. Yellow arrows in (B): empty voids; white arrows in (B): voids filled with carbonate mineral. A to D: BSE micrographs.

Figures 3 to 5 and A3 depict calcite microstructure and texture along cross-sections through the shell wall. We scanned the entire width of the shell wall and large sections of the chamber wall with EBSD (e.g., Figs. 3B, 4). The organization pattern of the crystals is illustrated with EBSD maps; we present two EBSD scans for each specimen. We measured at least four scans per specimen and, in most cases, covered all chambers that were cut. The corresponding texture patterns are presented with pole figures with individual data points (Figs. 3, 4) or with their density distributions (Fig. 5, A3). We use the term

'texture' in accordance with material science terminology, rather than as it is used in biological sciences. Crystal co-orientation strength (the MUD value) is given for entire EBSD scans and is presented at the density distributions of the c- and a*-axes orientation data (Figs. 5, A3). We compare the MUD value of the modern/pristine shell to the MUD value of the fossil shells. The MUD values are calculated for comparable data volumes; the data volumes used are specified in the relevant figures (Figs. 5, A3).
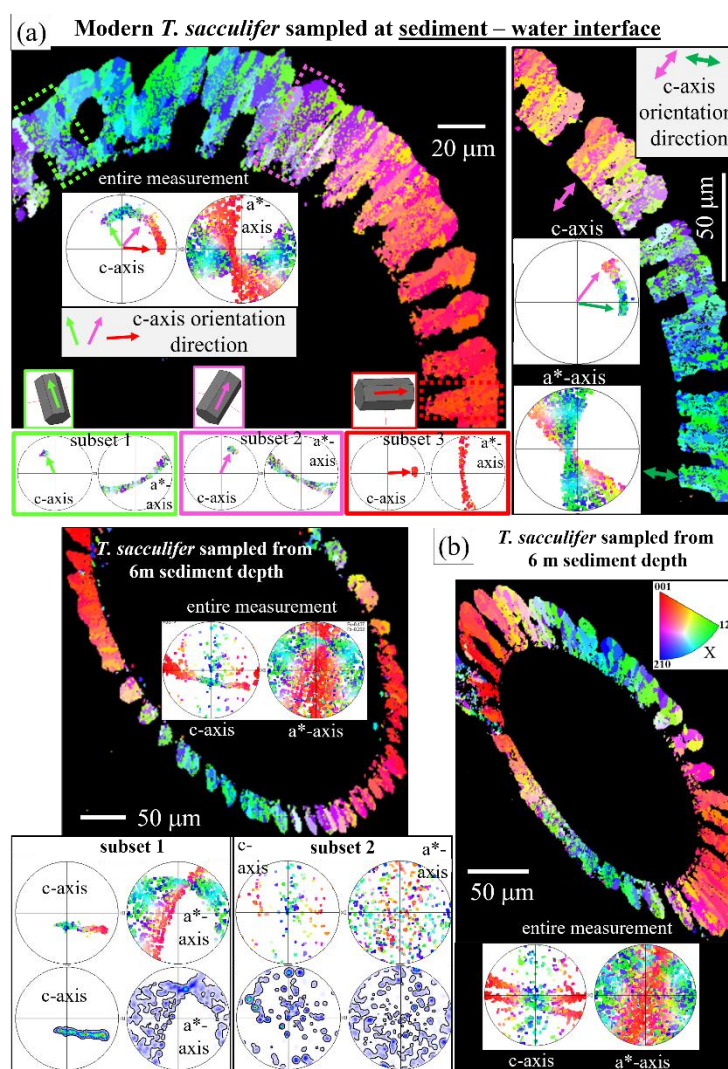
Figure 3. EBSD maps and corresponding pole figures visualizing the microstructure and texture of the *T. sacculifer* shells. A: the shell-wall of a modern/pristine *T. sacculifer* specimen, B: the shell-wall of a fossil *T. sacculifer* specimen, sampled at 6m sediment depth. Arrows in (A) indicate c-axis orientation direction in the EBSD maps as well as in the pole figures. For the left-hand side EBSD map and pole figure, we show the entire measurement as well as subsets (subsets 1, 2, 3) and visualize with these (i) the orientation of calcite c-axis relative to the surface of the chamber wall and (ii) its rotation with the curvature of the chamber wall. This characteristic is intrinsic for rotaliid shells (Fig. 3A of this study and e.g., Sancho Vaquer et al. (2025b)). Note the structured and directed c- and a*-axes orientation pattern of the calcite crystals that form the modern/pristine shell. This characteristic is best observable in the pole figures. B: For the shell sampled at 6m sediment depth, we observe some characteristics of the

modern/pristine *T. sacculifer* microstructure and texture in the maps and pole figures. Nonetheless, we find also additional crystal orientations (see the pole figures of subset 1 and 2 for the shell shown left-hand side measurement in (B)). These do not have the structured distribution of calcite c- and a*-axis orientation (subset 2 in 3B)), but a random pattern in c- and a*-axes orientation distribution. The used color code is given in (B).
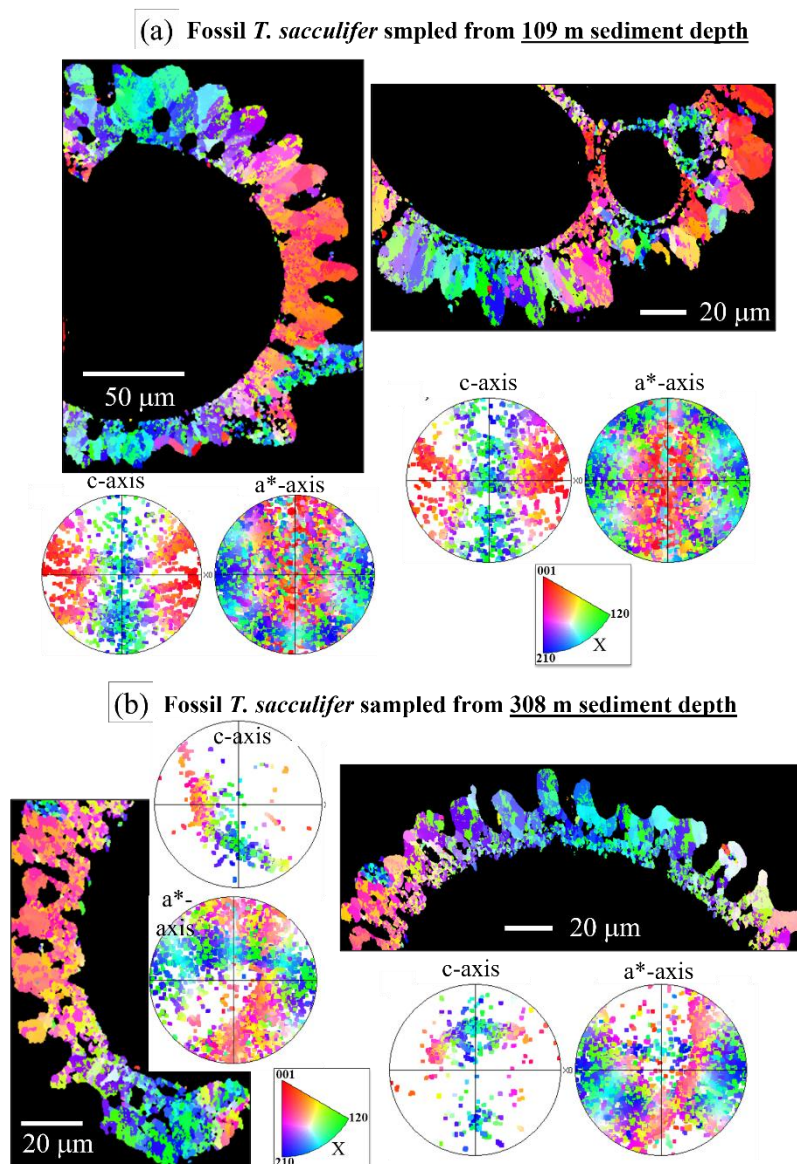
285

(a) Fossil *T. sacculifer* smpled from <u>109 m sediment depth</u>

(b) Fossil *T. sacculifer* sampled from <u>308 m sediment depth</u>

Figure 4. EBSD maps and corresponding pole figures visualizing the microstructure and texture of fossil *T. sacculifer* shells. A: the fossil *T. sacculifer* specimen sampled at 109m sediment depth. B: the fossil *T. sacculifer* specimen, sampled at 308m sediment depth. The used color code is given in (A) and (B). An increase in patchiness of the colors in the EBSD maps is well observable. From the pole figures, an increase in randomly oriented crystals can be observed. Compare the pole figures shown in Fig. 3A with the pole figures shown in Fig. 4A.
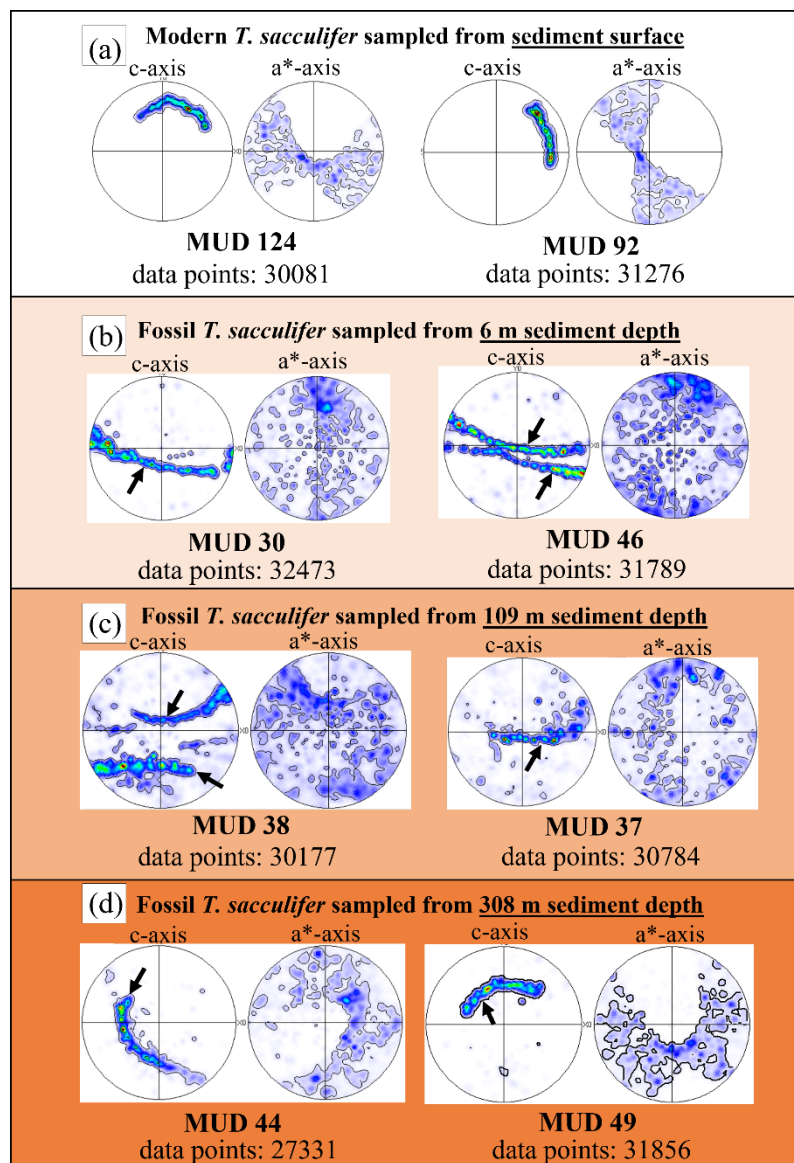
Figure 5. Juxtaposition of texture patterns and crystal co-orientation strengths (expressed with MUD values) for the investigated modern/pristine and fossil *T. sacculifer* specimens. For further measurements, see Fig. A3. We observe an increase in crystal co-orientation strength for the calcite of the modern/pristine shell (A), relative to the calcite of the fossil shells (B to D). For the calculation of the MUD values, we used comparable crystal orientation data volumes; the latter are given below the pole figures as data points. We find traces of the pristine crystal orientation signature for all fossil shells (black arrows in the c-axis pole figures in Fig. 5B to D). However, as shown in the pole figures, we also find a large volume of randomly oriented calcite crystallites.

The microstructure of the modern/pristine shell and that of the three fossil shells specimens are different (EBSD maps in Figs. 3 and 4). For all microstructures (modern/pristine, fossil), we see a wide range in color, indicating a wide range of crystal orientations. For the *modern/pristine specimen* (Fig. 3A) and, to some degree, for the *fossil specimen sampled at 6m sediment depth* as, we find a smooth transformation from one color into the other, thus, a smooth change in orientation

13

from one crystal to the other. Regarding the microstructure of the *fossil specimens* sampled at 109m and 308m (Fig. 4), we

305 still observe a wide range in colour in the EBSD maps, but also an increase in the patchiness of the colors (see, e.g., the EBSD maps shown in Fig. 4B). A patchiness in color hints to an abrupt change in orientation between adjacent crystals.

The pole figures for the modern/pristine shell (Fig. 3A) highlight the texture pattern that is specific for modern/pristine *T. sacculifer* shells (this study). This texture pattern is also observed for the shells of other modern/pristine Rotaliida (Lastam et al., 2023a, b; Sancho Vaquer et al., 2025b). We find that calcite c-axis orientation is perpendicular to

310 the surface of the shell and that it rotates with the curvature of the chamber (see arrows in Fig. 3A, which indicate the direction of the c-axis orientation). The orientation of calcite crystallites in modern/pristine *T. sacculifer* as well as in other rotaliid shells is strongly directional (see pole figures in Fig. 3A, for the entire measurement). A random scatter in calcite c- and a*-axis orientation is not (almost not) observed. Hence, the modern/pristine shell comprises very few randomly oriented crystals.

315 For the fossil shell sampled at 6m depth we find a comparable texture pattern to the modern/pristine shell (see pole figures in Fig. 3B, for the entire measurement). We observe the pristine *T. sacculifer* texture pattern (pole figures for subset 1 in Fig. 3B) but also some additional crystal orientations (pole figures for subset 2 in Fig. 3B). These are not directional but rather, random. We also find the aforementioned texture pattern for the fossil shells that were sampled at 109m and 308m sediment depths (Fig. 4). For the latter shells, we observe some traces of the pristine *T. sacculifer* texture but also a marked

320 addition of, more or less, randomly oriented crystals (Fig. 4).

When summarizing the structural attributes observed for the modern/pristine and for fossil shells with FE-SEM imaging (Figs. 1 to 5, A3), we see a comparability in quality of shell surface structure. With EBSD maps, we observe some difference in shell microstructure. However, when the texture patterns are considered (see the pole figures), we find a significant difference between the calcite texture of the modern/pristine shell and that of the fossil shells (Figs. 5, A3). We detect a

325 stringent arrangement of calcite c- and a*-axes orientation distributions and the coupling of the latter to an increased crystal co-orientation strength (MUD value). These two structural characteristics are significantly less well developed in the fossil shells (compare the pole figures of Fig. 5A to those shown in Fig. 5B to D). For the fossil shells, we observe the presence of randomly oriented crystals, accompanied by a decrease in crystal co-orientation strength (Figs. 5, A3).

Figure 6 highlights the misorientations between adjacent shell crystals for the modern/pristine and for the fossil shells. This

330 is also compared in Fig. 7. These are obtained from our EBSD measurements and are given with relative frequency-misorientation angle diagrams. We show two diagrams for each specimen. Well observable for all shells, whether modern/pristine or fossil, is the marked peak at 60° misorientation relative to the other misorientations measured with the EBSD scans. The peak at 60° misorientation is the 60°-<001>-calcite-twin misorientation (Schmahl et al., 2025). The latter is most pronounced for the modern/pristine shell (Fig. 6A) and least pronounced for the shell taken at 308m sediment depth

335 (Fig. 6D). The relative frequency of the 60° misorientation peak for the modern/pristine shell is about 0.7 for a binning of 2. This value was observed for the modern/pristine specimens sampled from all sampling locations. Thus, almost the entire modern/pristine *T. sacculifer* shell consists of twinned calcite. The relative frequency value of the 60° misorientation peak of

the fossil shells scatters between 0.5° and 0.3°, for a binning of 2 (Fig. 6). Thus, the fossil shells still contain some twinned calcite. However, the amount of the twinned crystals is lower relative to the amount of twinned crystals that comprise the
340   modern/pristine shells. Fig. A4 highlights the misorientations up to 59°. We show two misorientation diagrams per specimen. For all shells, irrespective of whether these are modern/pristine or fossil, we find, in addition to the 60° misorientation, further low-angle misorientations. These are low for the modern/pristine shell (Fig. A4A) and increased for the fossil shells (Fig. A4B to C).
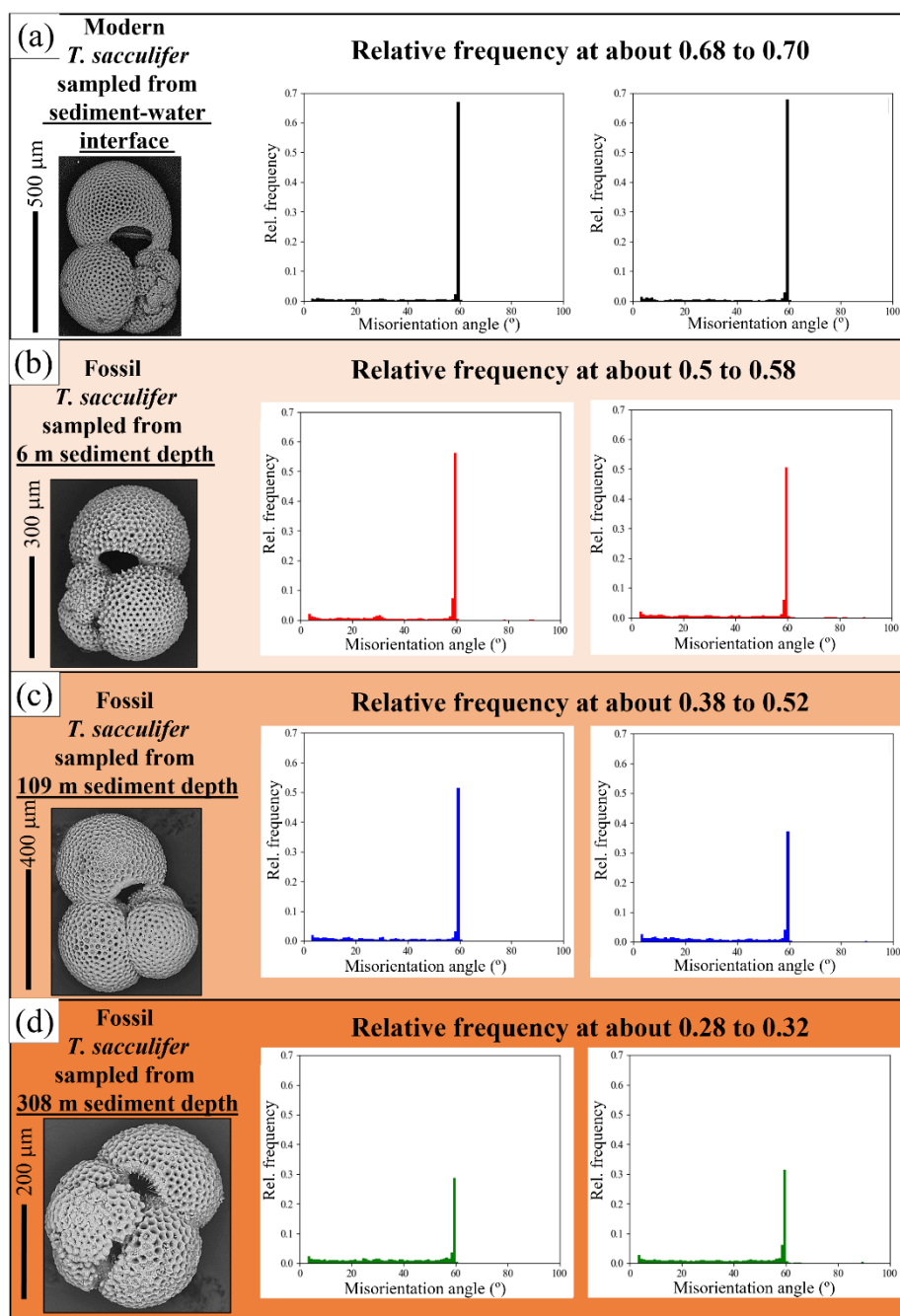
Figure 6. Relative frequency versus misorientation angle diagrams for a modern/pristine and for the three fossil *T. sacculifer* shells (A to D). Note the presence of the 60° misorientation peak for all shells. The latter indicates the twinned nature of the calcite that forms the shell. We observe: (i) a significant difference in the relative frequency of the 60° misorientation peak between the modern/pristine and the fossil specimens and (ii) a decrease of the relative frequency of the 60° misorientation with an increase of the sampling depth.
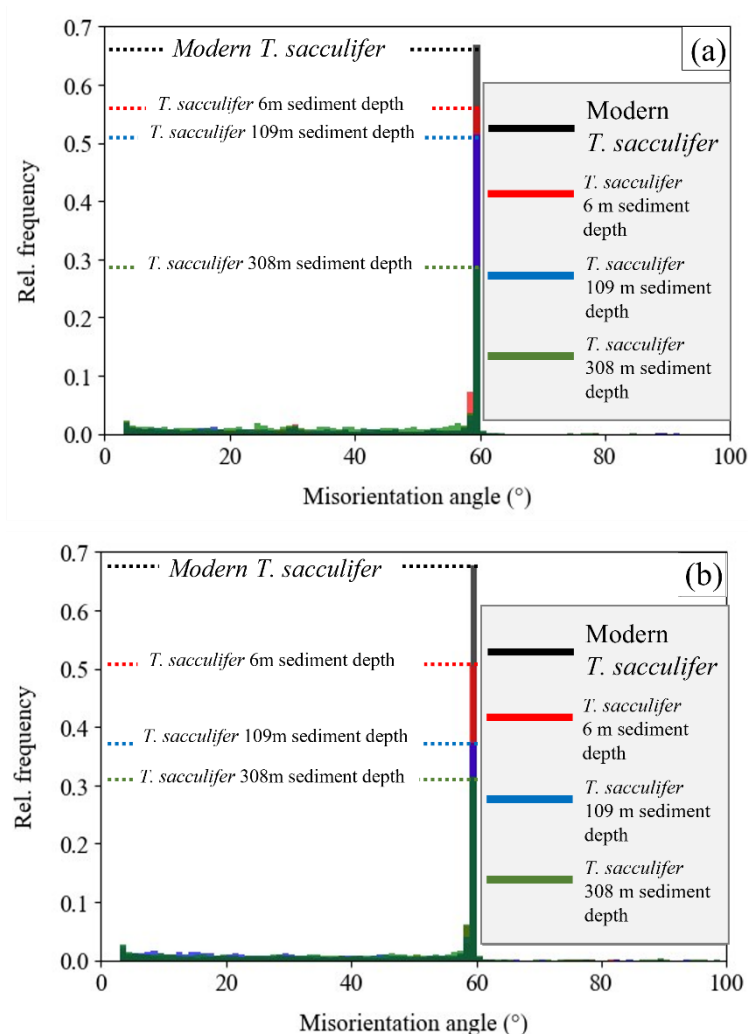
Figure 7. Comparison of the frequency of the 60°-<001>-calcite-twin-misorientation between the modern/pristine and the fossil *T. sacculifer* shells. The highest frequency of the 60° misorientation peak is observed for the modern/pristine shell, the lowest for the most overprinted shell (A, B). Note that the frequency of the 60° misorientation peak for the most overprinted shell is not zero, it has a relative frequency of about 0.3°.

In summary, the 60°-<001>-calcite-twin misorientation is strongest for the modern/pristine specimen. It is less marked for the fossil specimens and decreases in frequency with an increase in depth of the sampling site. The low-angle misorientations are lowest in frequency for the modern/pristine specimen, relative to those of the fossil specimens. These structural characteristics indicate addition of reprecipitated secondary calcite to the organism-secreted primary shell calcite.

17

4 Discussion

4.1 Criteria that document the overprint of the pristine shell

The aim of the present study is to highlight the difference in crystallite/crystal structure (morphology, size, mode of orientation) between fossil overprinted shells with only minor change of the microstructure and the modern/pristine analogue at preservation of an intact shell surface for *T. sacculifer* shells. We define structural directives, deduced from electron backscatter diffraction measurements, to demonstrate shell overprint and thus, change in crystallographic aspects of foraminiferal Ca-carbonate crystals.

Highlighting submicrometer-scale structural change of the shell crystals is of main importance. It has been shown that the oxygen isotope composition of foraminifera shells changes variably without any observable modification of the shell surface and/or its internal structure (Bernard et al., 2017; Chanda et al., 2019; Kozdon et al., 2018; Wycech et al., 2018). Nonetheless, the authors used SE, BSE imaging, EDS measurements and NanoSIMS mapping for demonstrating internal structural change of foraminifera shells (e.g. Bernard et al. 2017). As described in the introduction, we obtain large volumes of measured crystallographic axes orientation data with EBSD. EBSD measurements not only enable the determination of crystal orientation information and thus crystal microstructure, but also many other and different structural attributes of the crystallized material in question (Schwartz et al., 2000). Hence, we gain the possibility to pinpoint structural modification of the archival biological hard tissue with EBSD. This can then be used for geochemical proxy determination. Depending on the space resolution of the EBSD scan, the used acceleration voltage and the mode of data evaluation, we can detect changes in crystallographic attributes of crystals, routinely, as low as a few hundred nanometers, down to 200 nanometers (Casella et al., 2018b; Griesshaber et al., 2025; Hoerl et al., 2024b). With this, we obtain an improved structural characterization of the archive and an increase the accuracy of the selected proxy. We can therefore enhance the accuracy of climate and environment reconstruction.

Nonetheless, an important requirement of the proposed analytical approach is that the modification of the fossil archive shell/crystal structure has to be determined relative to the internal shell/crystal structure of a modern/pristine species analogue. This requirement is fulfilled here. All shells that we investigated in this study were *T. sacculifer* shells. We characterized modern/pristine *T. sacculifer* shells from different localities and with many EBSD measurements per species (Figs. A1, A2). Care was taken that the modern/pristine shells were sampled from the water, in particular from traps. For comparison, we deliberately used in one case a modern/pristine shell that was sampled from the sediment surface. However, we observed similar crystallographic attributes for the shell crystals for all investigated modern/pristine specimens, irrespective if these were sampled from traps or from the sediment surface. The modern/pristine shells analyzed in this study were never in contact with any diagenetic fluids. In contrast, all investigated fossil shells were sampled from sedimentary deposits and from different depths, partly from great depths (308m). Thus, it can be assumed that the investigated fossil shells were overprinted by the fluids that circulate within the sediments and were exposed to temperatures and pressures that prevailed at the different depths.

We aim to define criteria that document the modification of the pristine *T. sacculifer* shell crystal structure. These are crystal microstructure, crystal texture, the 60°-<001>-calcite-twin-related misorientation and the low-angle misorientations (Figs. 3, 395 4, A5). All these criteria are based on crystallographic axes orientation measurements and the evaluation of these. As shell formation with twinned calcite is an intrinsic structural attribute for modern/pristine benthic and planktonic Rotaliida (Lastam et al., 2023a, b; Sancho Vaquer et al., 2025b; Schmahl et al., 2025), the presence and frequency of the 60°-<001>-calcite-twin misorientation signal is a main criterion not only for indicating the overprint of the shell, but also for a possible assessment of the degree of overprint (Figs. 6, 7). For all investigated modern/pristine *T. sacculifer* shells, the frequency of 400 the 60°-<001>-misorientation peak scatters between 0.68 to 0.71, at a binning of 2°. In the most overprinted fossil *T. sacculifer* shell, we still find some twinned calcite as the frequency of the 60°-<001>-misorientation signal is about 0.3° at a binning of 2° (Figs. 6, 7). Our study showed that the frequency of the 60°-<001>-calcite-twin misorientation peak decreases with an increasing depth of the sampling site (Fig. 6D). This is an indication of an addition of non-biogenic crystals to the shells and recrystallization of the twinned biogenic calcite to untwinned inorganic calcite. Both latter processes generate 405 untwinned crystals. These are not systematically misoriented to each other, unlike the twinned crystals (through the 60°-<001>-misorientation), but are randomly misoriented to each other.

The addition of misoriented crystals to the fossil shells is also evident from other EBSD results. We find differences in the frequency of the low-angle misorientations between the modern/pristine and the three fossil samples (Fig. A4). In the fossil shells, the frequency of the low-angle misorientations is increased relative to the frequency of the low-angle 410 misorientations in the modern/pristine shell. The calcite that is generated at shell secretion is the primary calcite, while the calcite that forms through the diagenetic overprint processes is the secondary calcite (e.g., Forjanes et al. 2022). Laboratory-based experiments simulating overprint of Ca-carbonate shell material demonstrated that, in the course of the overprint process, the organic substance, present in the shells is destroyed first (Casella et al., 2017, 2018a; Casella, 2019; Forjanes et al., 2022). Herewith, space is generated in the hard tissue and allows for the circulation of diagenetic fluids within the shells 415 (Casella et al., 2017, 2018a, b; Casella, 2019; Forjanes et al., 2022). Depending on constrains, such as Ca-carbonate microstructure, organic substance fabric, overprint-fluid composition, temperature and pressure at the overprint process (Casella et al., 2018a; Casella, 2019), the circulating fluids dissolve to different degrees and speeds the <u>primary shell Ca-carbonate</u>. At a later stage of the overprint process, the dissolved Ca-carbonate becomes reprecipitated in voids and cavities within the shells and at its proximal and distal surface as <u>secondary Ca-carbonate</u>. The aforementioned overprint process is 420 known as coupled dissolution-reprecipitation and is active in the Earth crust on many length and time scales (Putnis, 2002, 2009). Thus, an increase of low-angle misorientations in fossil *T. sacculifer* shells relative to the frequency of the low-angle misorientations in the modern/pristine shell is an indication for formation of secondary calcite through coupled dissolution-reprecipitation.

While the microstructure of the primary *T. sacculifer*-secreted calcite is organism-controlled and has a characteristic texture 425 (Figs. 5A, A3A), the microstructure and texture of the secondary calcite is not organism-regulated; it is controlled by inorganic precipitation and recrystallization. For these, the orientation direction of the secondary calcite crystals is not

directed. It is random (see the difference in texture pattern for subsets 1 and 2 in Fig. 3B). It has been shown in laboratory experiments for mollusk shell Ca-carbonate that at shell dissolution and carbonate reprecipitation, there is no structural epitaxy between the primary shell crystals and the secondary precipitates (Casella et al., 2018a, b; Forjanes et al., 2022). Thus, there is no epitaxy between the orientation of the calcite crystals of the pristine foraminiferal shell and the orientation of the calcite crystals that form at overprint within the shell and at the surface of the shell. The increased patchiness of the colors in the EBSD maps of the fossil shells (e.g., EBSD maps shown in Fig. 4) is an indication for the latter.

430

We see formation of secondary calcite with an increase of low-angle misorientations in the fossil shells and, in particular, with the difference in texture patterns between the modern/pristine and the fossil shells. The texture pattern of modern/pristine *T. sacculifer* shells is constrained by the *T. sacculifer* microstructure. As described in the results section, in the modern/pristine *T. sacculifer* shells calcite c-axis orientation is perpendicular to chamber surface and rotates stringently with the curvature of the chamber wall. Thus, in the modern/pristine *T. sacculifer* shell the mode of calcite crystal orientation is far from random. It cannot be random, it has to be directed. In the fossil shells we find a large abundance of randomly oriented calcite crystals (e.g., subset 2 in Fig. 3B, Fig. 4A). These crystals are not secreted by the organism but are produced and deposited via the coupled dissolution-reprecipitation overprint process.

435

440

In essence, the 60°-<001>-calcite-twin misorientation signal, the low-angle misorientations and the texture patterns demonstrate that in the fossil shells we find calcite generated by two processes:

(i)   primary calcite formed and deposited through secretion and

(ii)   secondary calcite formed through dissolution and deposited through precipitation.

445

The 60°-<001>-calcite-twin misorientation signal is a very important structural criterion for demonstrating disturbance of the rotaliid calcite microstructure. It is metabolism-produced and is intrinsic for the Rotaliida. Sancho Vaquer et al. 2025a showed that the frequency of the 60°-<001>-calcite-twin misorientation peak of *Amphistegina lesonii* (d'Orbigny, 1830) and *Amphistegina lobifera* (Larsen, 1976) is reduced when the ambient water is polluted with Cd^{2+} or Pb^{2+}. In the most overprinted *T. sacculifer* shell the 60°-<001> misorientation peak has a frequency of about 0.3°, for the used histogram binning of 2°. Thus, the degree of overprint was not strong enough to erase all primary, metabolism-related, calcite. We still find twinned calcite in the most overprinted *T. sacculifer* shell.

450

In summary, our study shows that at more or less intact shell surface and a not too strongly disturbed crystal microstructure, shell overprint can still be pin pointed. The evaluation of crystallographic axes orientations allows for the determination of a plethora of structural attributes of the crystallized material in question. In this study, we use and discuss three structural attributes in addition to shell calcite microstructure: the 60° misorientation, the low-angle misorientations, and the crystal texture. These are structural markers, not just for identifying diagenetic overprint in shells, but also for the assessment of the strength of the overprint.

455

4.2 Shell crystal morphology, size, microstructure and texture

460 In the section above, we discussed the application of EBSD measurements and data evaluation for identifying criteria that demonstrate a modification in shell structure at external influence. However, for a comprehensive characterization of the lack of overprint or for the determination of the strength of the overprint, it is beneficial to substantiate the findings of crystal orientation measurements with results obtained from submicrometer scale imaging. We aim to integrate results obtained from measurements with results obtained from imaging. The latter is discussed in the subsequent sections.

465 ### 4.2.1 The modern/pristine shells

Crystal shape, size, and mode of interlinkage of modern/pristine Rotaliida shells is specific and distinct to the crystals that form the hard tissues of other Ca-carbonate producing marine invertebrates. While brachiopod and mollusk shell crystals have regular morphologies and consistent sizes and forms for a particular microstructure such as spicules, folia, laths, fibers, tablets, prisms or columns (Checa et al., 2025; Hoerl et al., 2024a, b; Sancho Vaquer et al., 2025c; Simonet Roda et al.,
470 2021), rotaliid foraminiferal shell crystals have fractal-dendritic morphologies and varying sizes. The crystals of rotaliid shells are fibrillary to platy (Fig. 8 this study, Fig. 3B in Lastam et al. (2023a) and Fig. 2C, E in Sancho Vaquer et al. (2025b)). Foraminiferal shell crystal formation starts with the secretion of nanometer-sized fibrils within the organic network of the POS. This is observed in *Pulleniatina obliquiloculata* (Parker and Jones 1865), *Neogloboquadrina dutertrei* (d'Orbigny 1839), *Globigerina glutinata* (Egger 1893), *Candeina nitida* (d'Orbigny 1839), and *T. sacculifer* (Fig. 8E this
475 study, Fig. 2E in Sancho Vaquer et al. (2025b)). With continued shell growth these nanofibrils agglomerate and generate sheaf-shaped, elongated, crystal entities (Fig. 8A, D, E this study, Fig. 4C in Lastam et al. (2023a), Fig. 5A, B in Lastam et al. (2023b), Fig. 2C, E in Sancho Vaquer (2025b)). With further growth, the sheaf-shaped crystal units as well as the comprising fibrillary crystallites increase in size. Towards distal outer surface, a change in crystal morphology takes place. The nanofibrils that prevail at the POS develop to large and platy crystals (Fig. 8A to C this study and Fig. 4A, B in Lastam
480 et al. (2023a). An array of platy crystals seams the distal rim of the shell (this study; Lastam et al. 2023a, b; Sancho Vaquer et al. 2025b). In modern/pristine foraminifera shells, the platy crystals are convoluted and interlaced and are arranged more or less in parallel (Fig. 8A, B, C). In modern/pristine foraminifera shells the platy crystals can be discriminated from each other (Fig. 8B, C this study, Fig. 4B in Lastam et al. (2023a)). For modern/pristine *T. sacculifer* shells, we find that fibrillary crystal units seam both sides of the POS (Fig. 8D, E) and that an array of sheaf-shaped crystals forms the shell layer
485 proximal to the POS (black dots in Fig. 8D). This is not always the case. The crystals that form the shell layer proximal to the POS in *P. obliquiloculata* are blocky and have euhedral morphologies (Figs. 2C in Lastam et al. (2023a)).
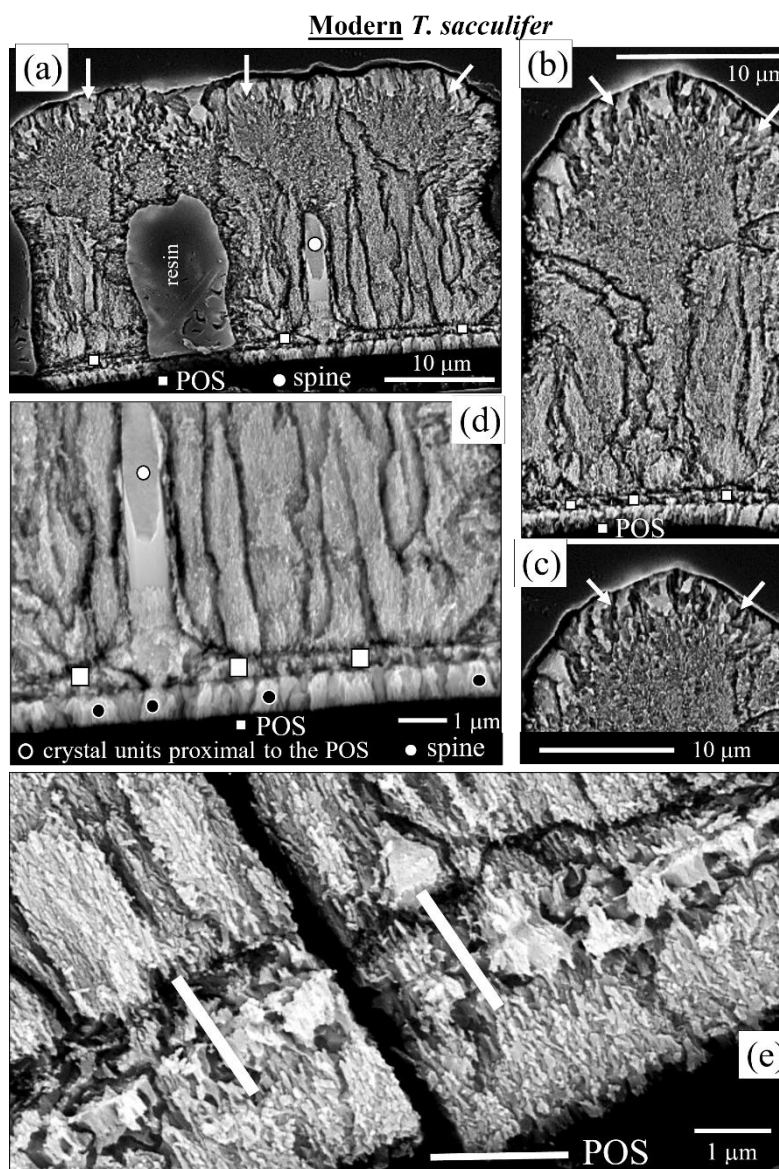
Modern *T. sacculifer*

Figure 8. Cross-sections depicting the internal structure of the modern/pristine *T. sacculifer* shell wall along the distal and proximal side of the POS (A, D, E). See the fibrous nature of the crystallites and highly irregular morphology of the calcite crystals that comprise modern/pristine *T. sacculifer* shells (e.g., (D), (E)). The POS is well observable (D). In *T. sacculifer* shells, the crystallites proximal to the POS have also a fibrous morphology, just as the crystallites distal to the POS (E). These fibrous crystallites accumulate to crystal units along both sides of the POS (D, E). White arrows in (A), (B) and (C) point to an assembly of platy calcite crystals that seam the outer surface of the shell wall. Note, in the modern/pristine shell these crystals are detached from each other. A to E: BSE micrographs.

22

4.2.2 The fossil shells

The shell sampled at 109m sediment depth

Even though the 60°-<001>-calcite-twin misorientation peak and the texture motif indicate that the shell sampled at 109m sediment depth experienced some diagenetic overprint, we find also well-developed signs for the preservation of the pristine shell structure (Fig. 9). We see well the distribution of the organic substance within the shell (white arrows in Fig. 9A, C, D, F, G). Hence, the organic substance is not yet decomposed by diagenesis. We can also discriminate quite well the course of the POS in the shell (Fig. 9B). Nonetheless, we find a first sign of overprint, namely the amalgamation of the platy crystals at the distal rim of the shell (white arrows in Fig. 9E) and hence, the elimination of small-angle grain boundaries by recrystallization and/or dissolution/reprecipitation. For the platy crystals to amalgamate, secondary calcite needs to precipitate. Thus, the rim along the distal surface of the shell sampled at 109m sediment depth consists of the primary calcite of the platy crystals and the secondary calcite that compacts the latter.

The shell sampled at 308m depth

SE and BSE imaging of the internal structure and of the crystals that comprise the shell sampled at 308m sediment depth (Figs. 10-13) demonstrates significant structural change of the shell wall crystals: the addition of secondary calcite to both shell surfaces as well as the deposition of secondary calcite within the shell. The platy crystals are not only amalgamated at the distal shell rim (yellow arrows in Fig. 10B) but are also covered by inorganic calcite overgrowth (white arrows in Fig. 10A to C). Figures 11 and 12B highlight shell structure change at the proximal surface of the shell. We find deposition of secondary calcite within the POS and at the amalgamation of the fibrils. The latter causes the compaction of the shell (Figs. 11, 12B). In addition, we see recrystallization of the sheaf-shaped entities proximal to the POS by rhombohedral calcite crystals (see yellow and black stars in Fig. 12) and the more or less complete loss of the original POS structure (yellow and white dots in Fig. 12). While the POS is well observable in modern/pristine *T. sacculifer* shells and to some degree, even in the shell sampled at 109m sediment depth (Figs. 8, 9), its structure is lost through secondary calcite deposition and recrystallization in the shell sampled at 308m depth (Fig. 11, 12B).

In addition to secondary calcite deposition at the distal and proximal surface of the shell, we observe secondary calcite deposition within the shell sampled at 308m sediment depth (Figs. 2B, C, 13B, C). BSE images highlight the sites where the organic substance in the shell became decomposed (yellow arrows in Figs. 2B, 13C) and the sites where newly-formed mineral precipitated in the newly-created voids (white arrows in Figs. 2B, 13C). In essence, we find a profound difference in crystal size, morphology and appearance in the internal structure of the most overprinted shell compared to that of the modern/pristine shell (Figs. 2, 13).

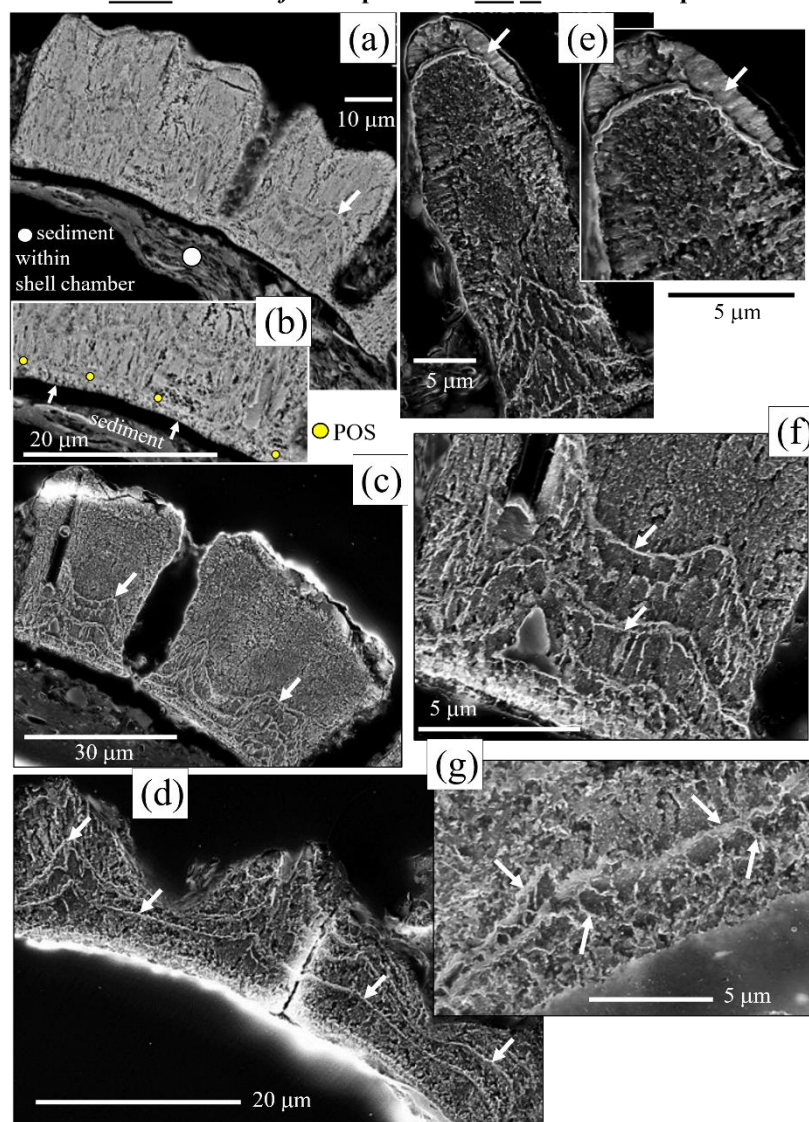**Fossil *T. sacculifer* sampled from 109 m sediment depth**

Figure 9. SE micrographs of cross-sections of the fossil *T. sacculifer* shell sampled at 109m sediment depths. Well visible is the presence of organic substance within the shell (white arrows in (A), (C), (D), (F), (G)). The course of the POS is quite well visible (A). Reprecipitated crystal formation is not observed proximal to the POS (B). Nonetheless, we find the amalgamation of the platy crystals that seam the outer rim of the modern/pristine shells (white arrows in (E)). At the latter process, the small-angle grain boundaries become eliminated by dissolution and recrystallization. A to F: SE micrographs.

530

Fossil *T. sacculifer* sampled from <u>308</u> <u>m</u> sediment depth
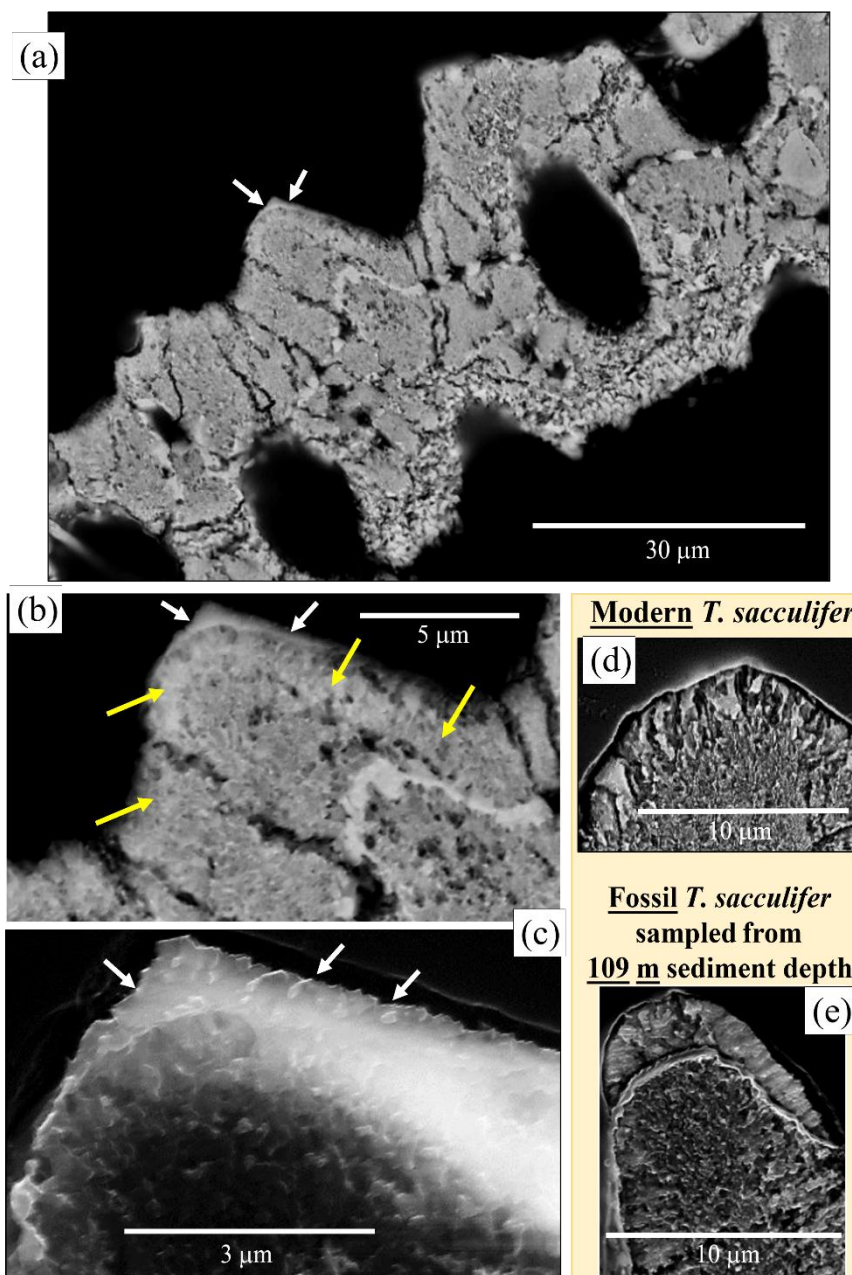
Figure 10. Recrystallization of calcite at distal shell wall surface (white arrows in A to C). The shell was sampled at 308m sediment depth. The array of platy crystals that seam the pristine shell wall surface (D) is destroyed through amalgamation (yellow arrows in (B)) and a cap, consisting of reprecipitated, inorganic calcite (white arrows in A to C). The latter crystals are deposited on top of the amalgamated platy crystals (white arrows in (C)). D: the modern/pristine *T. sacculifer* shell with the seam of platy crystals. E: the fossil *T. sacculifer* shell sampled at 109m sediment depth. Note the already amalgamated platy crystals at distal shell surface. A, B: BSE micrographs: C to E: SE micrographs.

535
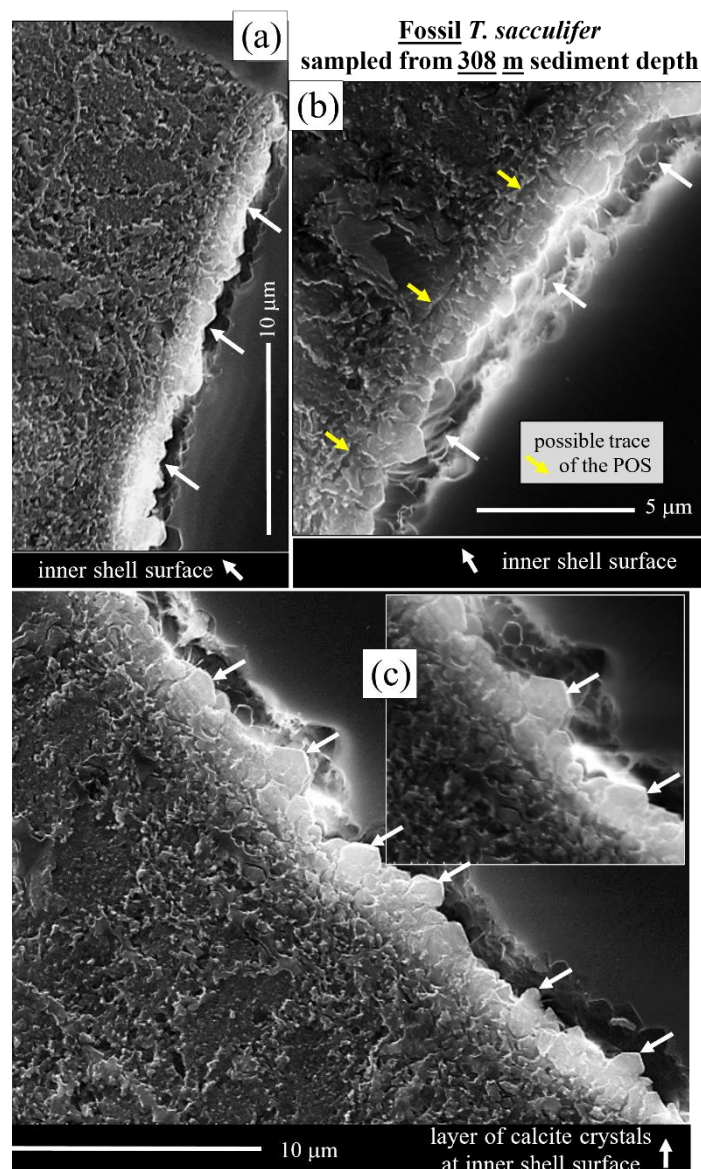
Figure 11. SE micrographs of cross-sections visualizing the proximal shell wall surface and slight traces of the POS of a fossil *T. sacculifer* specimen sampled at 308m sediment depth. White arrows in (A) to (C) point to a thin layer of calcite crystals that blanket the inner, proximal, shell surface of the fossil shell. Note the difference in calcite crystal morphology and size between these calcite crystals (white arrows in A to C) and the fibrous crystallites and crystals that form the proximal surface of the modern/pristine shell (Fig. 8A, D, E). The seam of calcite crystals along the proximal surface of the fossil shell is recrystallized calcite. These develop of the crystal units that, in the pristine shell, have a fibrous microstructure (Figs. 2A, 8D). Yellow arrows in (B) indicate the trace of the POS that was present in the unaltered shell. (A) to (C): SE micrographs.
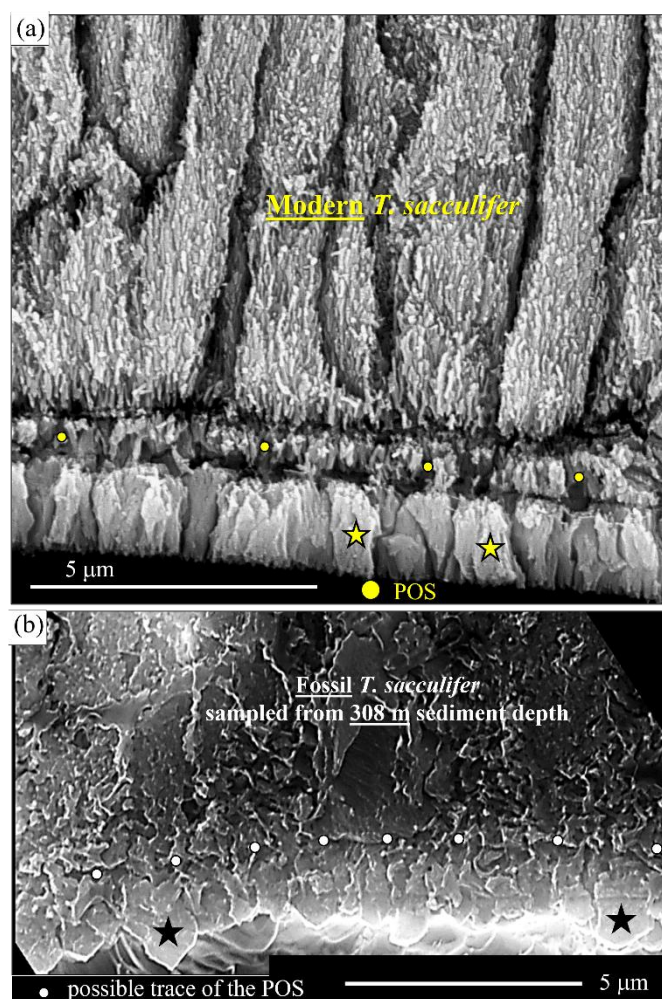
Figure 12. Juxtaposition of crystal/crystallite morphology, size and organization between the pristine (A) and the fossil *T. sacculifer* shell (B). A: BSE, B: SE micrograph. We find: (i) a striking difference in crystal morphology, (ii) a striking difference in the appearance of the POS, (iii) in particular, a striking difference in crystal morphology along the proximal surface of the shell and (iv) an absence of organic substance in the overprinted shell (B), relative to the presence of organic substance within the modern/pristine shell (A). In BSE micrographs mineralized substance is light-colored, organic substance is dark colored.

550
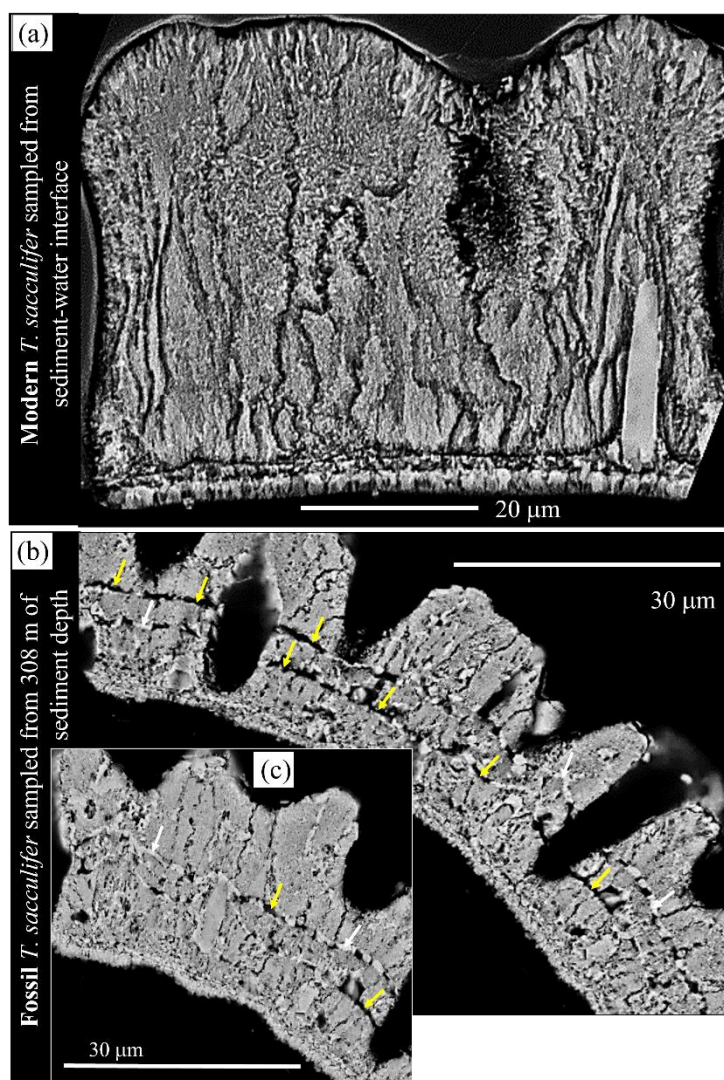
Figure 13. Juxtaposition of internal shell wall structure between the pristine (A) and the fossil *T. sacculifer* shell (B, C). A: BSE micrograph; B: SE micrograph. See the line of horizontal cavities (yellow arrows in (B) and (C)). These are in part empty (yellow arrows). They are, however, often filled with secondary, reprecipitated, calcite (white arrows in (B), (C)).

From the structural results obtained in this study, we can conclude that the fossil shells sampled at 6m and 109m sediment depth are little to moderately overprinted, while the fossil shell sampled at 308m sediment depth is substantially overprinted. For the latter, we find a change in shell crystal shape, size, and morphology, and the addition of secondary calcite to the primary calcite at shell surfaces and to inner shell sections. We find decomposition of shell-derived organic substance and recrystallization of the primary calcite. It should be kept in mind that all these structural changes are observed for a shell that has a well-preserved, intact shell surface (Fig. 1D).

5 Conclusion

Carbonates, irrespective of whether these are biogenic or abiogenic, are reactive minerals and undergo change between the time of their formation and their analysis (Arvidson and Morse, 2014). These changes are of chemical or structural nature
570 and induce the modification of the information that becomes incorporated into the carbonates at their secretion and/or deposition (Arvidson and Morse, 2014; Fantle et al., 2020; Immenhauser et al., 2016; Swart, 2015). The incorporated information reflects the environmental conditions at the time of carbonate formation and is acquired with proxies. However, the problem is that the fidelity of the proxies strongly depends on the preservation state of the archive. Depending on the quality of the latter, the environmental information can be just slightly modified or completely distorted.

575 In this contribution, we highlight the application of a microdiffraction technique (EBSD), associated data evaluation and complemented with submicrometer scale SE and BSE imaging for tracing the change of Ca-carbonate hard tissue structure with an increasing degree of diagenetic overprint. As foraminifera shells are major archives for paleoclimate and paleoenvironment reconstruction, we chose to examine the shells of the rotaliid species *T. sacculifer*. We investigated the microstructure, texture, and crystallographic properties of shell calcite of overprinted fossil shells, in comparison to the shell
580 of modern/pristine analogues. We draw the following conclusions from the gained results:

1. Shell surface appearance does not indicate any overprint.
2. Shell microstructure of the fossil shells is not significantly different to the shell microstructure of the pristine/modern analogue.
3. Diagenetic overprint can be traced with other structural and additional crystallographic attributes:

585   i. *The texture pattern of shell calcite*. There is not only a strong difference in crystal texture between the modern/pristine and the fossil shells, but also a change in calcite texture with an increasing degree of diagenesis. As the pole figures show (Figs. 3, 4), we see more or less random crystal orientations with an increasing degree of diagenesis formation relative to the modern/pristine shell.

   ii. *The 60°-<001>-calcite-twin misorientation peak*. 60°-<001>-calcite-twin formation is strongly
590   developed in modern/pristine *T. sacculifer* shells (Figs. 5A, A3A). The calcite-twin-related misorientation signal decreases with an increasing degree of diagenetic overprint (Figs. 5B to D, A3B to D). This indicates that abiogenic calcite is deposited within the shell and at the shell surface with an increasing degree of overprint.

   iii. *The low-angle misorientations*. The difference in the frequency of low-angle misorientations between
595   the modern/pristine and the fossil shells shows that inorganic calcite becomes deposited at/within the shells with diagenetic overprint.

   iv. *Secondary calcite deposition.*

   a. *Crystal amalgamation*. *Elimination of small-angle grain boundaries by recrystallization or dissolution/reprecipitation*. The fossil shell, sampled at 109m depth shows the amalgamation of

600   the platy crystals at its distal surface. In modern/pristine shells the platy crystals are detached from each other. In the fossil shell, the array of platy crystals forms a conglomerate. The conglomerate consists of the platy crystals and secondary calcite.

      Amalgamation also takes place of fibrils and of the sheaf-shaped crystals. The latter happens for the crystals below the POS, at the proximal surface of the fossil shells. For the shell sampled at a
605   depth of 308m, there is also a transformation of calcite crystal morphology from fibril-comprising units to blocky-euhedral crystal and a development of angles between calcite faces that are representative of inorganic calcite.
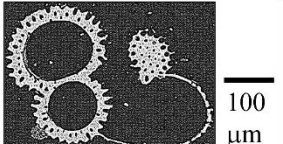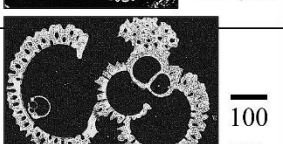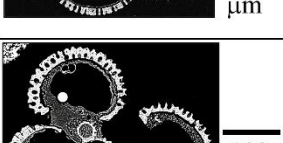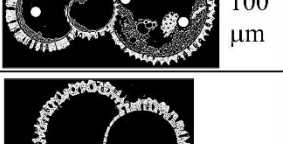
      b. *Abiogenic crystal deposition in voids within the shells*. With ongoing diagenesis, the organic substance decays and voids form within the shells. These permit diagenetic fluid circulation and
610   deposition of non-biogenic calcite.

    4. Based on the set of applied analytical tools we can conclude that all investigated fossil shells show signs of overprint. The overprint-derived change is minor for the shell sampled at a depth of 6m. It is severe for the shell sampled at 308m depth. For the latter, we observe a change in calcite texture, a significant alteration in crystal morphology, and the crystallization of secondary calcite within the shell.

615 Our study shows that minor to moderate diagenetic overprint of foraminifera shells can unequivocally be traced and proved with the combination of: (i) EBSD measurements, (ii) in-depth EBSD data evaluation and (iii) submicrometer-scale imaging of shell crystal structure and organic substance prevalence of chemically etched and chemically fixed shell surfaces. These can be used even for specimens with intact surfaces. For tracing diagenetic overprint in an archive, it is necessary to combine imaging with measurement techniques. The EBSD technique is perfectly suited for the latter, as the conveyed information is
620 solely based on measurements. These allow the calculation of criteria and parameters that can be used for identifying diagenetic overprint. With this study, we suggest to develop the EBSD technique for the definition of structural markers that allow the detection of shell structure change by diagenesis.
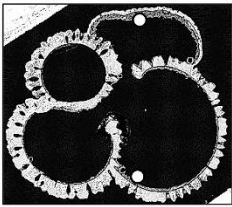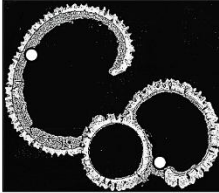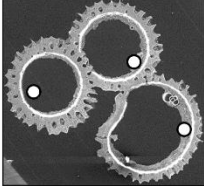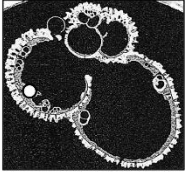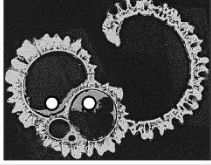
6 Appendix

Provenance	Analytical technique used for shell structure characterization	BSE Image
Modern *T. sacculifer* Eastern Atlantic Ocean sediment trap	EBSD	100 µm
Modern *T. sacculifer* Honjo, East Pacific sediment trap	EBSD	100 µm
Modern *T. sacculifer* Honjo, East Pacific sediment trap	EBSD	100 µm
Modern *T. sacculifer* Carribbean Sea sediment surface	EBSD	100 µm
Modern *T. sacculifer* Honjo, East Pacific sediment trap	Etching	100 µm
Fossil *T. sacculifer* Ceara Rise Central Atlantic Ocean 109 m burial depth burial age: 3.1 Ma	Etching	100 µm
Fossil *T. sacculifer* Ceara Rise Central Atlantic Ocean 308 m butial depth burial age: 15.9 Ma	Etching	100 µm

Figure A1. Table listing the provenance of the investigated modern/pristine and fossil *T. sacculifer* specimens, the applied characterization technique and the surfaces of the cut and investigated shell cross-sections depicted with BSE micrographs. The white dots in some of the micrographs point to sediment accumulations in the shell chambers.

31

Provenance	Analytical technique used for shell structure characterization	BSE Image
Fossil *T. sacculifer* Ceara Rise Central Atlantic Ocean 6m burial depth burial age: 0.127 Ma	EBSD	100 µm
Fossil *T. sacculifer* Ceara Rise Central Atlantic Ocean 6 m burial depth burial age: 0.127 Ma	EBSD	100 µm
Fossil *T. sacculifer* Ceara Rise Central Atlantic Ocean 15 m burial depth burail age: 0.329 Ma	EBSD	100 µm
Fossil *T. sacculifer* Ceara Rise Central Atlantic Ocean 109 m burial depth Burial age: 3.1 Ma	EBSD	100 µm
Fossil *T. sacculifer* Ceara Rise Central Atlantic Ocean 308 m burial depth burial age: 15.9 Ma	EBSD	100 µm

○ Sediment within shell chamber

Figure A2. Table listing the provenance of the investigated modern/pristine and fossil *T. sacculifer* specimens, the applied characterization technique and depicting with BSE micrographs the surfaces of the cut and investigated shell cross-sections. The white dots in some of the micrographs point to sediment accummulations in the shell chambers.

630

Figure A3. The difference in texture pattern and crystal co-orientation strength between modern/pristine and fossil *T. sacculifer* shells.
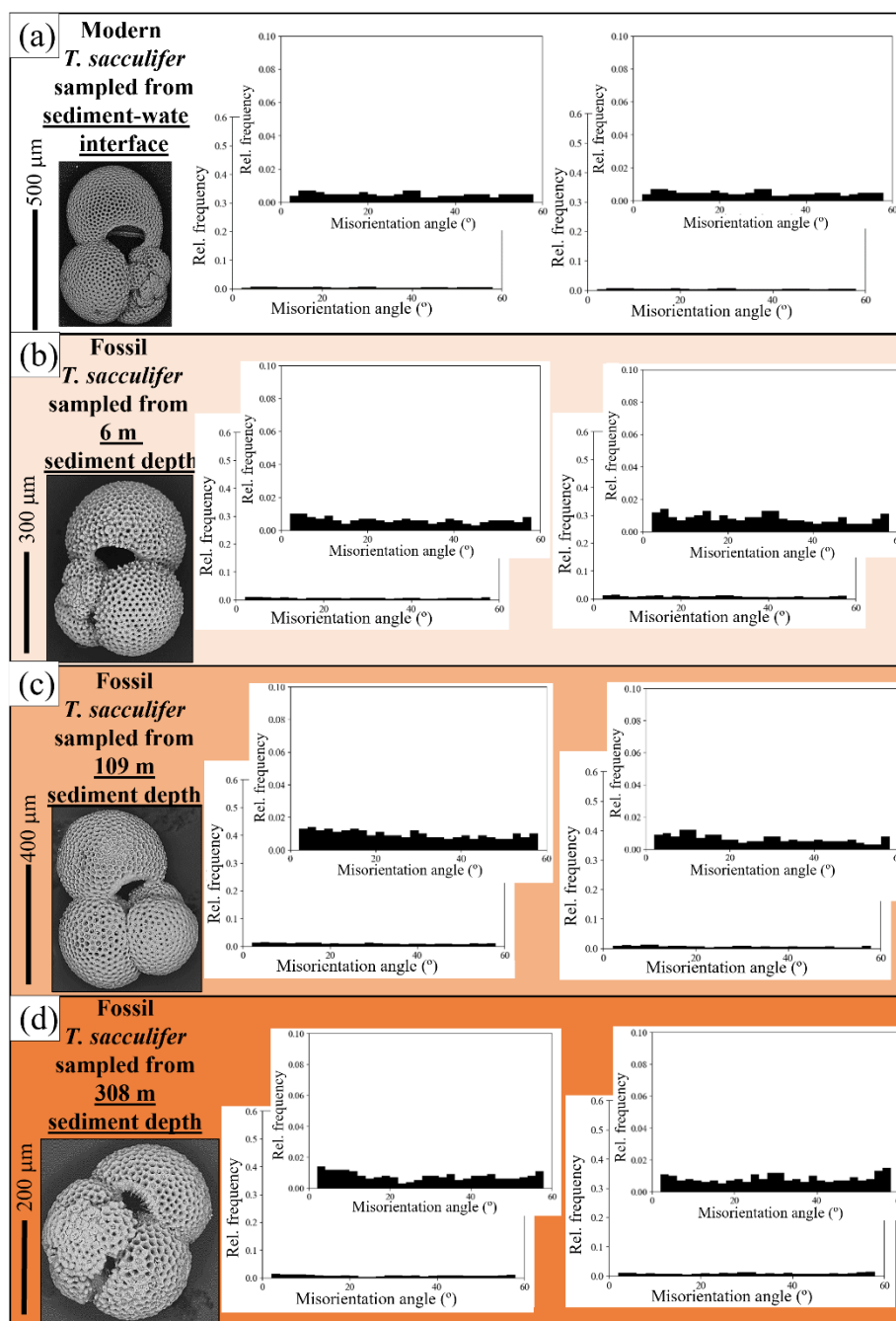
Figure A4. Compilation of low-angle misorientations for the modern/pristine and for the fossil *T. saccullifer* shells. We show the frequencies of the misorientations between 5° and 59°, thus, without the 60° misorientation. We find that: (i) the frequencies of the low-angle misorientations for the modern/pristine, on the one hand, and the frequencies of the low-angle misorientations for the fossil shells, on the other, differ (compare the frequencies shown in (A) with the frequencies shown in (B to D)). ii. We do not find a marked difference in the relative frequency of the low-angle misorientations between the fossil shells.
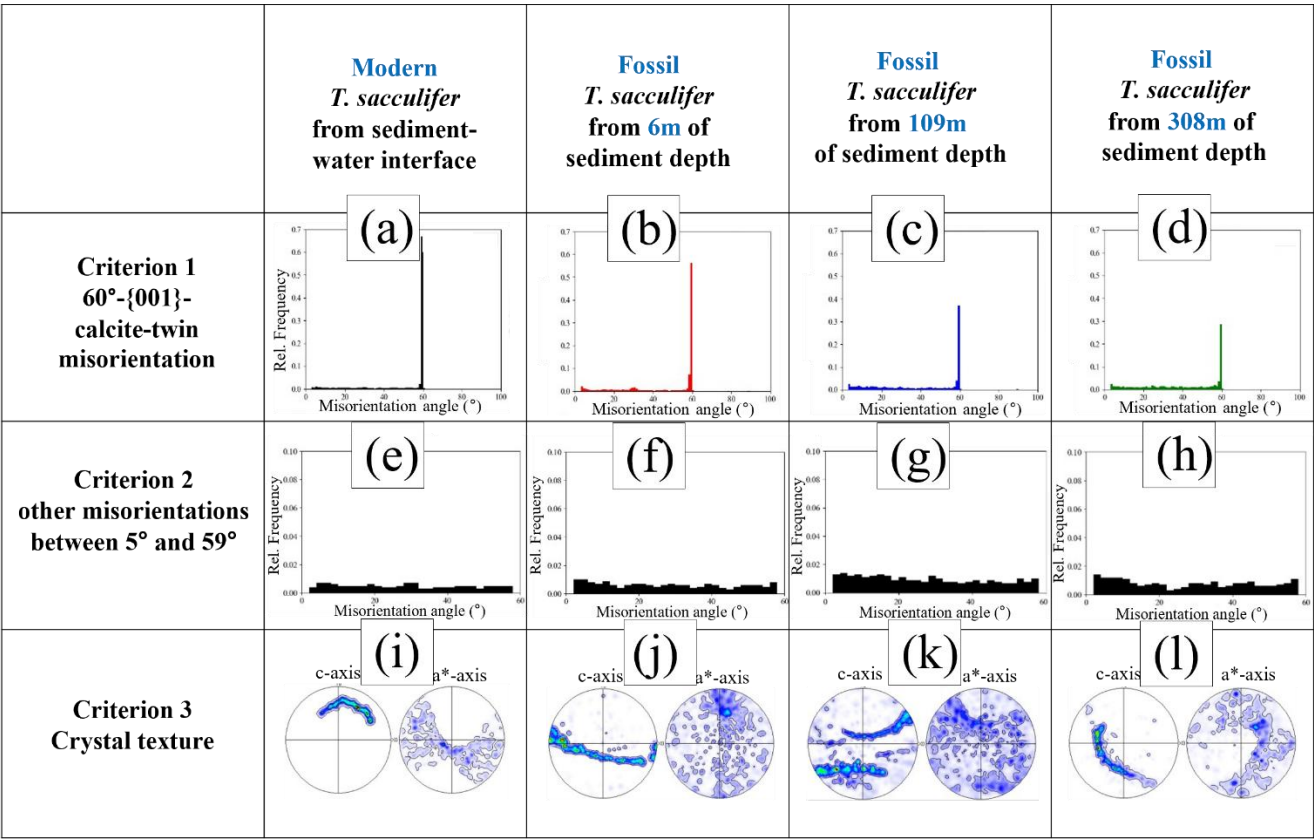
645

Figure A5. Structural criteria, obtained from EBSD measurements, for the modern/pristine and the fossil *T. sacculifer* shells, that indicate structural change of the shell-wall crystals. The structural state of the modern/pristine shell wall crystals is used as reference for the structural state of the fossil shell crystals. Prime indicators for overprint are the misorientations between the crystals and the crystallites that comprise the shells ((A) to (H)) and the motif of the texture patterns ((I) to (L)). As pristine rotaliid shells have a very specific microstructure and texture pattern (this study; Lastam et al. 2023a, b,; Sancho Vaquer et al. 2025b), change of the latter by external perturbance is easily detected (e.g., Sancho Vaquer et al. 2025a) and can well be demonstrated with EBSD measurements. The investigated modern/pristine *T. sacculifer* shells are from the sediment-water interface and were not in contact with the seafloor sediment.

Data availability

655   Data is available upon request.

Author contributions

ASV and EG evaluated the data and worked on the manuscript. XY prepared the samples. JM, MS and MK provided the
660   samples and contributed to discussion. WWS worked on the manuscript and contributed to discussion.

Competing interests

The authors declare no competing interests.

Disclaimer

Copernicus Publications remains neutral with regard to jurisdictional claims made in the text, published maps, institutional
665   affiliations, or any other geographical representation in this paper. While Copernicus Publications makes every effort to
include appropriate place names, the final responsibility lies with the authors. Views expressed in the text are those of the
authors and do not necessarily reflect the views of the publisher.

Financial support

References

Akhtar, A. A., Cruger Ahm, A.-S., and Higgins, J. A.: Geochemical fingerprints of early diagenesis in shallow-water marine carbonates: Insights from paired $\delta^{44/40}$Ca and δ^{26}Mg values, Geochim. Cosmochim. Acta, 383, 57–69, https://doi.org/10.1016/j.gca.2024.08.002, 2024.

Almagro, I., Drzymała, P., Berent, K., Sainz-Díaz, C. I., Willinger, M. G., Bonarski, J., and Checa, A. G.: New Crystallographic Relationships in Biogenic Aragonite: The Crossed-Lamellar Microstructures of Mollusks, Cryst. Growth Des., 16, 2083–2093, https://doi.org/10.1021/acs.cgd.5b01775, 2016.

de Araújo, O. M. O., Aguilera, O., Machado, A. S., de Oliveira, D. F., Leitão, R. G., dos Anjos, M. J., and Lopes, R. T.: Analysis of Diagenetic Impacts on Foraminifera by X-Rays Techniques, X-Ray Spectrom., 54, 773–783, https://doi.org/10.1002/xrs.70012, 2025.

Arvidson, R. S. and Morse, J. W.: 9.3 - Formation and Diagenesis of Carbonate Sediments, in: Treatise on Geochemistry (Second Edition), edited by: Holland, H. D. and Turekian, K. K., Elsevier, Oxford, 61–101, https://doi.org/10.1016/B978-0-08-095975-7.00703-8, 2014.

Bassinot, F. C., Mélières, F., Gehlen, M., Levi, C., and Labeyrie, L.: Crystallinity of foraminifera shells: A proxy to reconstruct past bottom water $CO_3^=$ changes?, Geochem. Geophys. Geosystems, 5, https://doi.org/10.1029/2003GC000668, 2004.

Baumgartner-Mora, C.: Shell structure of fossil foraminifera studied by cathodoluminescence, Eur. Microsc Anal, 29–32, 1994.

Bernard, S., Daval, D., Ackerer, P., Pont, S., and Meibom, A.: Burial-induced oxygen-isotope re-equilibration of fossil foraminifera explains ocean paleotemperature paradoxes, Nat. Commun., 8, 1134, https://doi.org/10.1038/s41467-017-01225-9, 2017.

Brand, U.: Carbon, oxygen and strontium isotopes in Paleozoic carbonate components: an evaluation of original seawater-chemistry proxies, Chem. Geol., 204, 23–44, https://doi.org/10.1016/j.chemgeo.2003.10.013, 2004.

Brand, U., Logan, A., Hiller, N., and Richardson, J.: Geochemistry of modern brachiopods: applications and implications for oceanography and paleoceanography, Chem. Geol., 198, 305–334, https://doi.org/10.1016/S0009-2541(03)00032-9, 2003.

Buerger, M. J.: The Genesis of Twin Crystals, Am. Mineral., 30, 469–482, 1945.

Carpenter, S. J. and Lohmann, K. C.: δ^{18}O and δ^{13}C values of modern brachiopod shells, Geochim. Cosmochim. Acta, 59, 3749–3764, https://doi.org/10.1016/0016-7037(95)00291-7, 1995.

Casella, L. A.: Nano- and microstructural transformation processes during diagenesis of biogenic carbonates, Ph.D. Thesis, Ludwig-Maximilians Universität, Munich, Germany, 293 pp., 2019.

Casella, L. A., Griesshaber, E., Yin, X., Ziegler, A., Mavromatis, V., Müller, D., Ritter, A.-C., Hippler, D., Harper, E. M., Dietzel, M., Immenhauser, A., Schöne, B. R., Angiolini, L., and Schmahl, W. W.: Experimental diagenesis: insights into aragonite to calcite transformation of *Arctica islandica* shells by hydrothermal treatment, Biogeosciences, 14, 1461–1492, https://doi.org/10.5194/bg-14-1461-2017, 2017.

Casella, L. A., He, S., Griesshaber, E., Fernández-Díaz, L., Greiner, M., Harper, E. M., Jackson, D. J., Ziegler, A., Mavromatis, V., Dietzel, M., Eisenhauer, A., Veintemillas-Verdaguer, S., Brand, U., and Schmahl, W. W.: Hydrothermal

alteration of aragonitic biocarbonates: assessment of micro- and nanostructural dissolution–reprecipitation and constraints of diagenetic overprint from quantitative statistical grain-area analysis, Biogeosciences, 15, 7451–7484, https://doi.org/10.5194/bg-15-7451-2018, 2018a.

720 Casella, L. A., Griesshaber, E., Simonet Roda, M., Ziegler, A., Mavromatis, V., Henkel, D., Laudien, J., Häussermann, V., Neuser, R. D., Angiolini, L., Dietzel, M., Eisenhauer, A., Immenhauser, A., Brand, U., and Schmahl, W. W.: Micro- and nanostructures reflect the degree of diagenetic alteration in modern and fossil brachiopod shell calcite: A multi-analytical screening approach (CL, FE-SEM, AFM, EBSD), Palaeogeogr. Palaeoclimatol. Palaeoecol., 502, 13–30, https://doi.org/10.1016/j.palaeo.2018.03.011, 2018b.

725 Chanda, P., Gorski, C. A., Oakes, R. L., and Fantle, M. S.: Low temperature stable mineral recrystallization of foraminiferal tests and implications for the fidelity of geochemical proxies, Earth Planet. Sci. Lett., 506, 428–440, https://doi.org/10.1016/j.epsl.2018.11.011, 2019.

Charrieau, L. M., Rollion-Bard, C., Terbrueggen, A., Wilson, D. J., Pogge von Strandmann, P. A. E., Misra, S., and Bijma, J.: Controls on Lithium Incorporation and Isotopic Fractionation in Large Benthic Foraminifera, Minerals, 13, 127, https://doi.org/10.3390/min13010127, 2023.

730 Checa, A. G., Griesshaber, E., Salas, C., Angiolini, L., and Schmahl, W. W.: Biomineralization of mollusc and brachiopod shells, in: Biomineralization and Bioinspired Composites, vol. 1, edited by: Cölfen, H., World Scientific, 2025.

Cisneros-Lazaro, D., Adams, A., Guo, J., Bernard, S., Baumgartner, L. P., Daval, D., Baronnet, A., Grauby, O., Vennemann, T., Stolarski, J., Escrig, S., and Meibom, A.: Fast and pervasive diagenetic isotope exchange in foraminifera tests is species-dependent, Nat. Commun., 13, 113, https://doi.org/10.1038/s41467-021-27782-8, 2022.

735 Cornuault, P., Westerhold, T., Pälike, H., Bickert, T., Baumann, K.-H., and Kucera, M.: Nature and origin of variations in pelagic carbonate production in the tropical ocean since the mid-Miocene (ODP Site 927), Biogeosciences, 20, 597–618, https://doi.org/10.5194/bg-20-597-2023, 2023.

Crippa, G., Griesshaber, E., Checa, A. G., Harper, E. M., Simonet Roda, M., and Schmahl, W. W.: Orientation patterns of aragonitic crossed-lamellar, fibrous prismatic and myostracal microstructures of modern *Glycymeris* shells, J. Struct. Biol., 740 212, 107653, https://doi.org/10.1016/j.jsb.2020.107653, 2020a.

Crippa, G., Griesshaber, E., Checa, A. G., Harper, E. M., Simonet Roda, M., and Schmahl, W. W.: SEM, EBSD, laser confocal microscopy and FE-SEM data from modern *Glycymeris* shell layers, Data Brief, 33, 106547, https://doi.org/10.1016/j.dib.2020.106547, 2020b.

Edgar, K.: Foraminifera and Their Applications, Marine Biology Research, 11, 223–224, 745 https://doi.org/10.1080/17451000.2014.946424, 2015.

Edgar, K. M., Pälike, H., and Wilson, P. A.: Testing the impact of diagenesis on the δ^{18}O and δ^{13}C of benthic foraminiferal calcite from a sediment burial depth transect in the equatorial Pacific, Paleoceanography, 28, 468–480, https://doi.org/10.1002/palo.20045, 2013.

Elderfield, H., Vautravers, M., and Cooper, M.: The relationship between shell size and Mg/Ca, Sr/Ca, δ^{18}O, and δ^{13}C of 750 species of planktonic foraminifera, Geochem. Geophys. Geosystems, 3, 1–13, https://doi.org/10.1029/2001GC000194, 2002.

Fantle, M. S., Barnes, B. D., and Lau, K. V.: The Role of Diagenesis in Shaping the Geochemistry of the Marine Carbonate Record, Annu. Rev. Earth Planet. Sci., 48, 549–583, https://doi.org/10.1146/annurev-earth-073019-060021, 2020.

Fehrenbacher, J. S., Hupp, B. N., Branson, O., Evans, D., Foster, G. L., Glock, N., Thirumalai, K., and Wycech, J.: Individual foraminiferal analyses: a review of current and emerging geochemical techniques, J. Foraminifer. Res., 54, 312–331, https://doi.org/10.61551/gsjfr.54.4.312, 2024.

Floquet, N. and Vielzeuf, D.: Mesoscale twinning and crystallographic registers in biominerals, Am. Mineral., 96, 1228–1237, https://doi.org/10.2138/am.2011.3805, 2011.

Forjanes, P., Simonet Roda, M., Greiner, M., Griesshaber, E., Lagos, N. A., Veintemillas-Verdaguer, S., Astilleros, J. M., Fernández-Díaz, L., and Schmahl, W. W.: Experimental burial diagenesis of aragonitic biocarbonates: from organic matter loss to abiogenic calcite formation, Biogeosciences, 19, 3791–3823, https://doi.org/10.5194/bg-19-3791-2022, 2022.

Griesshaber, E., Schmahl, W. W., Ubhi, H. S., Huber, J., Nindiyasari, F., Maier, B., and Ziegler, A.: Homoepitaxial meso- and microscale crystal co-orientation and organic matrix network structure in *Mytilus edulis* nacre and calcite, Acta Biomater., 9, 9492–9502, https://doi.org/10.1016/j.actbio.2013.07.020, 2013.

Griesshaber, E., Sancho Vaquer, A., Checa, A. G., Salas, C., Harper, E. M., and Schmahl, W. W.: The textural motif of foliated calcite in Ostreoidea (Mollusca), Crystals, 15, 244, https://doi.org/10.3390/cryst15030244, 2025.

Gussone, N., Hönisch, B., Heuser, A., Eisenhauer, A., Spindler, M., and Hemleben, C.: A critical evaluation of calcium isotope ratios in tests of planktonic foraminifers, Geochim. Cosmochim. Acta, 73, 7241–7255, https://doi.org/10.1016/j.gca.2009.08.035, 2009.

Hahn, Th. and Klapper, H.: Twinning of crystals, in: International Tables for Crystallography, Online MRW, John Wiley & Sons, Ltd, Hoboken, NJ, USA, 393–448, https://doi.org/10.1107/97809553602060000644, 2006.

Hansen, H. J.: Shell construction in modern calcareous Foraminifera, in: Modern Foraminifera, edited by: Sen Gupta, B. K., Springer Netherlands, Dordrecht, 57–70, https://doi.org/10.1007/0-306-48104-9_4, 1999.

Heuser, A., Eisenhauer, A., Böhm, F., Wallmann, K., Gussone, N., Pearson, P. N., Nägler, T. F., and Dullo, W.-C.: Calcium isotope ($\delta^{44/40}$Ca) variations of Neogene planktonic foraminifera, Paleoceanography, 20, https://doi.org/10.1029/2004PA001048, 2005.

Hidayat, B., Sebayang, N. U. W., Jamilah, J., and Mahardika, A.: Brunauer-Emmett-Teller, Fourier-transform infrared, and scanning-electron-microscope analysis of biochar from marine organic waste, SAINS TANAH - J. Soil Sci. Agroclimatol., 22, 127–134, https://doi.org/10.20961/stjssa.v22i1.93314, 2025.

Hoerl, S.: Calcium carbonate biomaterials - architecture, design and nanomechanical properties of selected mollusc, brachiopod and echinoderm skeletal elements, PhD Thesis, Ludwig-Maximilians Universität, Munich, Germany, 2025.

Hoerl, S., Griesshaber, E., Checa, A. G., and Schmahl, W. W.: The biological crystals in Chamid bivalve shells: Diversity in morphology and crystal arrangement pattern, Crystals, 14, 649, https://doi.org/10.3390/cryst14070649, 2024a.

Hoerl, S., Micheletti, C., Amini, S., Griesshaber, E., Peharda, M., and Schmahl, W. W.: The difference in microstructure, texture and mechanical behaviour between *Glycymeris*, *Chama* and *Placopecten* myostraca, Materialia, 2024b.

Hoogakker, B., Ishimura, T., de Nooijer, L., Rathbun, A., and Schmiedl, G.: A review of benthic foraminiferal oxygen and carbon isotopes, Quat. Sci. Rev., 342, 108896, https://doi.org/10.1016/j.quascirev.2024.108896, 2024.

Hottinger, L.: The depth-depending ornamentation of some lamellar-perforate foraminifera, Symbiosis, 2006.

Immenhauser, A., Schöne, B. R., Hoffmann, R., and Niedermayr, A.: Mollusc and brachiopod skeletal hard parts: Intricate archives of their marine environment, Sedimentology, 63, 1–59, 2016.

790   Kogure, T., Suzuki, M., Kim, H., Mukai, H., Checa, A. G., Sasaki, T., and Nagasawa, H.: Twin density of aragonite in molluscan shells characterized using X-ray diffraction and transmission electron microscopy, J. Cryst. Growth, 397, 39–46, https://doi.org/10.1016/j.jcrysgro.2014.03.029, 2014.

Kozdon, R., Kelly, D. C., and Valley, J. W.: Diagenetic Attenuation of Carbon Isotope Excursion Recorded by Planktic Foraminifers During the Paleocene-Eocene Thermal Maximum, Paleoceanogr. Paleoclimatology, 33, 367–380,
795   https://doi.org/10.1002/2017PA003314, 2018.

Kramer, A., Herzschuh, U., Mischke, S., and Zhang, C.: Late glacial vegetation and climate oscillations on the southeastern Tibetan Plateau inferred from the Lake Naleng pollen profile, Quat. Res., 73, 324–335, https://doi.org/10.1016/j.yqres.2009.12.003, 2010.

Ku, T. C. W., Walter, L. M., Coleman, M. L., Blake, R. E., and Martini, A. M.: Coupling between sulfur recycling and
800   syndepositional carbonate dissolution: evidence from oxygen and sulfur isotope composition of pore water sulfate, South Florida Platform, U.S.A., Geochim. Cosmochim. Acta, 63, 2529–2546, https://doi.org/10.1016/S0016-7037(99)00115-5, 1999.

Lastam, J., Griesshaber, E., Yin, X., Rupp, U., Sánchez-Almazo, I., Heß, M., Walther, P., Checa, A., and Schmahl, W. W.: Patterns of crystal organization and calcite twin formation in planktonic, rotaliid, foraminifera shells and spines, J. Struct.
805   Biol., 215, 107898, https://doi.org/10.1016/j.jsb.2022.107898, 2023a.

Lastam, J., Griesshaber, E., Yin, X., Rupp, U., Sánchez-Almazo, I., Heß, M., Walther, P., Checa, A., and Schmahl, W. W.: The unique fibrilar to platy nano- and microstructure of twinned rotaliid foraminiferal shell calcite, Sci. Rep., 13, 2189, https://doi.org/10.1038/s41598-022-25082-9, 2023b.

Lipps, J. H.: Test Structure in Foraminifera, Annu. Rev. Microbiol., 27, 471–486,
810   https://doi.org/10.1146/annurev.mi.27.100173.002351, 1973.

Nagai, Y., Uematsu, K., Wani, R., and Toyofuku, T.: Reading the fine print: Ultra-microstructures of foraminiferal calcification revealed using focused ion beam microscopy, Front. Mar. Sci., 4, https://doi.org/10.3389/FMARS.2018.00067/PDF, 2018a.

Nagai, Y., Uematsu, K., Chen, C., Wani, R., Tyszka, J., and Toyofuku, T.: Weaving of biomineralization framework in
815   rotaliid foraminifera: implications for paleoceanographic proxies, Biogeosciences, 15, 6773–6789, https://doi.org/10.5194/bg-15-6773-2018, 2018b.

Nouet, J. and Bassinot, F.: Dissolution effects on the crystallography and Mg/Ca content of planktonic foraminifera *Globorotalia tumida* (Rotaliina) revealed by X-ray diffractometry, Geochem. Geophys. Geosystems, 8, https://doi.org/10.1029/2007GC001647, 2007.

820   Pearson, P. N.: Oxygen Isotopes in Foraminifera: Overview and Historical Review, Paleontol. Soc. Pap., 18, 1–38, https://doi.org/10.1017/S1089332600002539, 2012.

Piasecki, A., Bernasconi, S. M., Grauel, A.-L., Hannisdal, B., Ho, S. L., Leutert, T. J., Marchitto, T. M., Meinicke, N., Tisserand, A., and Meckler, N.: Application of clumped isotope thermometry to benthic foraminifera, Geochem. Geophys. Geosystems, 20, 2082–2090, https://doi.org/10.1029/2018GC007961, 2019.

825   Poirier, R. K., Gaetano, M. Q., Acevedo, K., Schaller, M. F., Raymo, M. E., and Kozdon, R.: Quantifying diagenesis, contributing factors, and resulting isotopic bias in benthic foraminifera using the foraminiferal preservation index: implications for geochemical proxy records, Paleoceanogr. Paleoclimatology, 36, e2020PA004110, https://doi.org/10.1029/2020PA004110, 2021.

Procter, F. A., Piazolo, S., John, E. H., Walshaw, R., Pearson, P. N., Lear, C. H., and Aze, T.: Electron backscatter
830   diffraction analysis unveils foraminiferal calcite microstructure and processes of diagenetic alteration, Biogeosciences, 21, 1213–1233, https://doi.org/10.5194/bg-21-1213-2024, 2024.

Putnis, A.: Mineral replacement reactions: from macroscopic observations to microscopic mechanisms, Mineral. Mag., 66, 689–708, https://doi.org/10.1180/0026461026650056, 2002.

Putnis, A.: Mineral Replacement Reactions, Rev. Mineral. Geochem., 70, 87–124, https://doi.org/10.2138/rmg.2009.70.3,
835   2009.

Putnis, A. and Austrheim, H.: Mechanisms of Metasomatism and Metamorphism on the Local Mineral Scale: The Role of Dissolution-Reprecipitation During Mineral Re-equilibration, in: Metasomatism and the Chemical Transformation of Rock: The Role of Fluids in Terrestrial and Extraterrestrial Processes, edited by: Harlov, D. E. and Austrheim, H., Springer, Berlin, Heidelberg, 141–170, https://doi.org/10.1007/978-3-642-28394-9_5, 2013.

840   Richards, R. P.: The Four Twin Laws of Calcite and How To Recognize Them, Rocks Miner., 74, 308–317, https://doi.org/10.1080/00357529909602559, 1999.

Sancho Vaquer, A.: Ca-carbonate crystal morphology and organization in single-celled protists, multi-celled invertebrates, and in biomimetic aggregates generated with microorganismal extracellular polysaccharides (EPS): differences and variability, Ph.D. Thesis, Ludwig-Maximilians Universität, Munich, Germany, 2026.

845   Sancho Vaquer, A., Griesshaber, E., Yin, X., Siccha, M., Ben-Eliahu, N., Herut, B., Rahav, E., Abramovich, S., Kucera, M., and Schmahl, W. W.: *Amphistegina lessonii* and *Amphistegina lobifera* shell microstructure, texture and twinning pattern reflect resilience to cadmium and lead, Sci. Rep., 15, 14617, https://doi.org/10.1038/s41598-025-94811-7, 2025a.

Sancho Vaquer, A., Griesshaber, E., Meilland, J., Fernández-Díaz, L., Yin, X., Lastam, J., de Nooijer, L., Kucera, M., and Schmahl, W. W.: Microstructure and texture of foraminiferal Ca-carbonate: the different biomineralization strategies of
850   Rotaliida, Robertinida, and Miliolida, Cryst. Growth Des., 25, 3274–3297, https://doi.org/10.1021/acs.cgd.4c01531, 2025b.

Sancho Vaquer, A., Griesshaber, E., Salas, C., Harper, E. M., Checa, A. G., and Schmahl, W. W.: The diversity of crystals, microstructures and texture that form Ostreoidea shells, Crystals, 15, 286, https://doi.org/10.3390/cryst15030286, 2025c.

Sandberg, P. A.: An oscillating trend in Phanerozoic non-skeletal carbonate mineralogy, Nature, 305, 19–22, https://doi.org/10.1038/305019a0, 1983.

855   Schmahl, W. W., Yin, X., Lastam, J., Griesshaber, E., Hoerl, S., Sturm, E., and Sancho Vaquer, A.: Statistical analysis of EBSD data confirms pronounced classical and non-classical pervasive crystallographic twinning in rotaliid foraminiferal calcite, Sci. Rep., 15, 14852, https://doi.org/10.1038/s41598-025-92636-y, 2025.

Schöne, B. R., Zhang, Z., Radermacher, P., Thébault, J., Jacob, D. E., Nunn, E. V., and Maurer, A.-F.: Sr/Ca and Mg/Ca ratios of ontogenetically old, long-lived bivalve shells (*Arctica islandica*) and their function as paleotemperature proxies,
860   Palaeogeogr. Palaeoclimatol. Palaeoecol., 302, 52–64, https://doi.org/10.1016/j.palaeo.2010.03.016, 2011.

Schwartz, A. J., Kumar, M., and Adams, B. L. (Eds.): Electron Backscatter Diffraction in Materials Science, Springer US, Boston, MA, https://doi.org/10.1007/978-1-4757-3205-4, 2000.

Simonet Roda, M., Ziegler, A., Griesshaber, E., Yin, X., Rupp, U., Greiner, M., Henkel, D., Häussermann, V., Eisenhauer, A., Laudien, J., and Schmahl, W. W.: Terebratulide brachiopod shell biomineralization by mantle epithelial cells, J. Struct.
865 Biol., 207, 136–157, https://doi.org/10.1016/j.jsb.2019.05.002, 2019.

Simonet Roda, M., Griesshaber, E., Angiolini, L., Rollion-Bard, C., Harper, E. M., Bitner, M. A., Milner Garcia, S., Ye, F., Henkel, D., Häussermann, V., Eisenhauer, A., Gnägi, H., Brand, U., Logan, A., and Schmahl, W. W.: The architecture of Recent brachiopod shells: diversity of biocrystal and biopolymer assemblages in rhynchonellide, terebratulide, thecideide and craniide shells, Mar. Biol., 169, 4, https://doi.org/10.1007/s00227-021-03962-4, 2021.

870 Spero, H. J.: Ultrastructural examination of chamber morphogenesis and biomineralization in the planktonic foraminifer *Orbulina universa*, Mar. Biol., 99, 9–20, https://doi.org/10.1007/BF00644972, 1988.

Spezzaferri, S., Kucera, M., Pearson, P. N., Wade, B. S., Rappo, S., Poole, C. R., Morard, R., and Stalder, C.: Fossil and genetic evidence for the polyphyletic nature of the planktonic foraminifera "globigerinoides", and description of the new genus trilobatus, PLOS ONE, 10, e0128108, https://doi.org/10.1371/journal.pone.0128108, 2015.

875 Stainbank, S., Kroon, D., de Leau, E. S., and Spezzaferri, S.: Using past interglacial temperature maxima to explore transgressions in modern Maldivian coral and *Amphistegina* bleaching thresholds, Sci. Rep., 11, 10267, https://doi.org/10.1038/s41598-021-89697-0, 2021.

Stewart, J. A., Gutjahr, M., Pearce, F., Swart, P. K., and Foster, G. L.: Boron during meteoric diagenesis and its potential implications for Marinoan snowball Earth δ^{11}B-pH excursions, Geology, 43, 627–630, https://doi.org/10.1130/G36652.1,
880 2015.

Stolper, D. A., Fischer, W. W., and Bender, M. L.: Effects of temperature and carbon source on the isotopic fractionations associated with O2 respiration for $^{17}O/^{16}O$ and $^{18}O/^{16}O$ ratios in *E. coli*, Geochim. Cosmochim. Acta, 240, 152–172, https://doi.org/10.1016/j.gca.2018.07.039, 2018.

Suzuki, M., Kim, H., Mukai, H., Nagasawa, H., and Kogure, T.: Quantitative XRD analysis of {1 1 0} twin density in
885 biotic aragonites, J. Struct. Biol., 180, 458–468, https://doi.org/10.1016/j.jsb.2012.09.004, 2012.

Swart, P. K.: The geochemistry of carbonate diagenesis: The past, present and future, Sedimentology, 62, 1233–1304, https://doi.org/10.1111/sed.12205, 2015.

Tyszka, J., Bickmeyer, U., Raitzsch, M., Bijma, J., Kaczmarek, K., Mewes, A., Topa, P., and Janse, M.: Form and function of F-actin during biomineralization revealed from live experiments on foraminifera, Proc. Natl. Acad. Sci. U. S. A., 116,
890 4111–4116, https://doi.org/10.1073/pnas.1810394116, 2019.

Veizer, J., Ala, D., Azmy, K., Bruckschen, P., Buhl, D., Bruhn, F., Carden, G. A. F., Diener, A., Ebneth, S., Godderis, Y., Jasper, T., Korte, C., Pawellek, F., Podlaha, O. G., and Strauss, H.: $^{87}Sr/^{86}Sr$, $\delta^{13}C$ and $\delta^{18}O$ evolution of Phanerozoic seawater, Chem. Geol., 161, 59–88, https://doi.org/10.1016/S0009-2541(99)00081-9, 1999.

Wendler, J. E., Wendler, I., Rose, T., and Huber, B. T.: Using Cathodoluminescence Spectroscopy of Cretaceous Calcareous
895 Microfossils to Distinguish Biogenic from Early-Diagenetic Calcite, Microsc. Microanal., 18, 1313–1321, https://doi.org/10.1017/S1431927612001353, 2012.

Wycech, J. B., Kelly, D. C., Kitajima, K., Kozdon, R., Orland, I. J., and Valley, J. W.: Combined Effects of Gametogenic Calcification and Dissolution on $\delta^{18}O$ Measurements of the Planktic Foraminifer *Trilobatus sacculifer*, Geochem. Geophys. Geosystems, 19, 4487–4501, https://doi.org/10.1029/2018GC007908, 2018.

900 Ye, F., Crippa, G., Angiolini, L., Brand, U., Capitani, G., Cusack, M., Garbelli, C., Griesshaber, E., Harper, E., and Schmahl, W.: Mapping of recent brachiopod microstructure: A tool for environmental studies, J. Struct. Biol., 201, 221–236, https://doi.org/10.1016/j.jsb.2017.11.011, 2018.

Ye, F., Jurikova, H., Angiolini, L., Brand, U., Crippa, G., Henkel, D., Laudien, J., Hiebenthal, C., and Šmajgl, D.: Variation in brachiopod microstructure and isotope geochemistry under low-pH–ocean acidification conditions, Biogeosciences, 16, 905 617–642, https://doi.org/10.5194/bg-16-617-2019, 2019.

Ye, F., Garbelli, C., Shen, S., and Angiolini, L.: The shell fabric of Palaeozoic brachiopods: patterns and trends, Lethaia, 54, 419–439, https://doi.org/10.1111/let.12412, 2021.

Yin, X., Griesshaber, E., Checa, A. G., Nindiyasari-Behal, F., Sánchez-Almazo, I., Ziegler, A., and Schmahl, W. W.: Calcite crystal orientation patterns in the bilayers of laminated shells of benthic rotaliid foraminifera., J. Struct. Biol., 231, 107707, 910 2021.

Zachos, J., Pagani, M., Sloan, L., Thomas, E., and Billups, K.: Trends, rhythms, and aberrations in global climate 65 Ma to present, Science, 292, 686–693, https://doi.org/10.1126/science.1059412, 2001.

Zachos, J. C., Stott, L. D., and Lohmann, K. C.: Evolution of Early Cenozoic marine temperatures, Paleoceanography, 9, 353–387, https://doi.org/10.1029/93PA03266, 1994.

915